Chromatin remodeling protein CHD4 regulates axon guidance of spiral ganglion neurons in developing cochlea

Jihyun Kim[1,2,*], Edward Martinez[1,2,*], Jingyun Qiu[2], Julie Zhouli Ni[3], Kelvin Y. Kwan[1,2]

[1]Keck Center for Collaborative Neuroscience and Stem Cell Research Center, Rutgers University, Piscataway, NJ 08854, USA

[2]Department of Cell Biology and Neuroscience, Rutgers University, Piscataway, NJ 08854, USA

[3] Department of Molecular Biology and Biochemistry, Rutgers University, Piscataway, NJ 08854, USA

* J.K. and E.M. contributed equally to this work.

Corresponding Author:

Kelvin Y. Kwan

Address: 604 Allison Road, D250 Nelson Labs, Piscataway, NJ 08854

Email: kwan@dls.rutgers.edu

Running Title: CHD4 axon guidance

Key Words: CHD4, spiral ganglion neurons, axon guidance, epigenetics, chromatin remodeling

Word Count:

Number of Figures: 6

Number of Tables: 3

Number of Supplemental Figures: 3

Number of Supplemental Table: 1

Abstract (202 words)

The chromodomain helicase binding protein 4 (CHD4) is an ATP-dependent chromatin remodeler. *De-novo* pathogenic variants of *CHD4* cause Sifrim-Hitz-Weiss syndrome (SIHIWES). Patients with SIHIWES show delayed development, intellectual disability, facial dysmorphism, and hearing loss. Many cochlear cell types, including spiral ganglion neurons (SGNs), express CHD4. SGNs are the primary afferent neurons that convey sound information from the cochlea, but the function of CHD4 in SGNs is unknown. We employed the Neurog1(Ngn1) CreERT^2 *Chd4* conditional knockout animals to delete *Chd4* in SGNs. SGNs are classified as type I and type II neurons. SGNs lacking CHD4 showed abnormal fasciculation of type I neurons along with improper pathfinding of type II fibers. CHD4 binding to chromatin from immortalized multipotent otic progenitor-derived neurons was used to identify candidate target genes in SGNs. Gene ontology analysis of CHD4 target genes revealed cellular processes involved in axon guidance, axonal fasciculation, and ephrin receptor signaling pathway. We validated increased *Epha4* transcripts in SGNs from *Chd4* conditional knockout cochleae. The results suggest that CHD4 attenuates the transcription of axon guidance genes to form the stereotypic pattern of SGN peripheral projections. The results implicate epigenetic changes in circuit wiring by modulating axon guidance molecule expression and provide insights into neurodevelopmental diseases.

Introduction

Congenital hearing loss syndromes are often associated with pathogenic genetic variants in a single gene. Hearing loss can be syndromic or non-syndromic. Syndromic hearing impairment is associated with clinical features in other organ systems, while non-syndromic hearing impairment has no discernable clinical abnormalities other than in the middle or inner ear. Syndromic hearing loss accounts for over 400 genetic syndromic hearing loss conditions (Toriello et al., 2004). The characteristics of syndromic hearing loss vary among the different syndromes and affect hearing in either one or both ears. The extent of hearing loss varies dramatically and can range from profound to mild. Different syndromes show distinct features of hearing loss at different sound frequencies. Improper development or dysfunction of the sensory cells and neurons of the inner ear correlates to many forms of syndromic hearing loss.

Mutations in genes that code for epigenetic modifiers can cause syndromic hearing loss. Pathogenic variants in DNA methyltransferases (DNMT1), histone methyltransferases (EHMT1, KMT2D), acetyltransferase (KAT6B), and the chromodomain helicase DNA binding (CHD) protein family are associated with hearing loss (Layman and Zuo, 2014). The CHD family of proteins mobilizes and rearranges nucleosomes to alter chromatin accessibility. Pathogenic variants in CHD4 and CHD7 are associated with Sifrim-Hitz-Weiss and CHARGE syndrome, respectively (Clapier et al., 2017; Micucci et al., 2015). Sifrim-Hitz-Weiss (SIHIWES) is an autosomal dominant intellectual developmental disorder with variable congenital abnormalities. Patients with SIHIWES show delayed development, intellectual disability, facial dysmorphism, and ear abnormalities, including hearing loss (Sifrim et al., 2016a; Weiss et al., 2016). Hearing loss in patients with SIHIWES is confounded by the potential function of CHD4 in many different inner ear cell types during development. In the mouse, the expression of CHD4 and components of the nucleosome remodeling and deacetylase (NuRD) complex are expressed in many cells in the cochlea sensory epithelium (Layman et al., 2013). CHD4 has been studied in the context of the NuRD complex (Tong et al., 1998; Xue et al., 1998; Zhang et al., 1998). Paralogs from six protein

families form the core NuRD complex (Millard et al., 2016; Torchy et al., 2015). Multiple paralogs from each protein family can form distinct NuRD complexes (Torrado et al., 2017). The ATP-dependent nucleosome remodeler CHD4 and the histone deacetylases (HDAC1, HDAC2) form the catalytic subunits. Other members include the methyl binding proteins (MBD2, MBD3), and structural subunits (MTA1, MTA2, MTA3, GATAD2A, GATAD2B, RBBP4, RBBP7). The NuRD complex is localized to active promoters and enhancers to attenuate transcription (Morra et al., 2012; Watson et al., 2012).

A decrease in transcription caused by the NuRD complex affects a myriad of cellular processes, including maintenance of cell identity, DNA damage repair, cell cycle progression, and cancer (Bornelov et al., 2018; Hosokawa et al., 2013; Hung et al., 2012; Pan et al., 2012; Polo et al., 2010; Xia et al., 2017; Yang et al., 2016). CHD4 binds to thousands of sites in the mammalian genome in a cell-type-specific manner, and studies show that CHD4 forms distinct protein complexes with NuRD-independent functions (Hoffmeister et al., 2017; Low et al., 2016). We employed a conditional knockout model to understand CHD4 function in developing spiral ganglion neurons (SGNs) and how the deletion of CHD4 contributes to hearing loss. SGNs are the primary afferent neurons in the cochlea that convey auditory signals from the sensory hair cells to the cochlear nucleus in the brainstem. Improper function of SGNs could result in sensorineural hearing loss. We examined *Chd4* function in SGNs using a transgenic mouse line harboring the Neurog1(Ngn1) CreER^{T2} (Koundakjian et al., 2007), *Chd4* conditional knockout (cKO) alleles (Williams et al., 2004) and a tdTomato reporter (Madisen et al., 2010).

Materials and Methods

Generation of *Chd4* conditional knockout mice

All procedures were based on institutional animal care, used committee research guidelines, and were done at Rutgers University. *Chd4*$^{tm1Kge/tm1Kge}$ (*Chd4* floxed*)* animals (RRID:MGI:3713386) were obtained from Dr. Katia Georgopoulos ((Williams et al., 2004). Neurog1(Ngn1) CreER^{T2} animals and Ai9 R26R tdTomato reporter animals were purchased from Jackson Laboratory (RRID:IMSR_JAX:008529 and RRID:IMSR_JAX:007909, respectively) (Koundakjian et al., 2007; Madisen et al., 2010). PCR genotyping was performed using the EconoTaq Plus Green 2X Master Mix (Lucigen) and primer pairs for wild-type and *Chd4* floxed alleles (Table 1). For Cre-induced excision of loxP-flanked exons that code for the ATPase domain of *Chd4*, a mixture of tamoxifen and β-estradiol was diluted in corn oil. β-estradiol was included to help alleviate the anti-estrogen effects of tamoxifen treatments. 1 mg of tamoxifen per 40 g of body weight was used on individual animals. Tamoxifen doses for pregnant female mice were adjusted for maternal body weight. Pregnant dams were gavaged with 0.25mg/40g of tamoxifen (Sigma #T5648) and 0.25µg/40g of β-estradiol (Sigma #E8875) daily on embryonic days (E) 8.5- 10.5 to induce Cre activity. For staging timed embryos, the morning that vaginal plugs were observed, pregnant female mice were considered carrying E 0.5 embryos.

Tissue fixation and preparation

Embryos or postnatal pups were sacrificed for inner ear dissection. After bisecting the mouse head, brain tissue was removed. The temporal bone was removed, and the inner ear was separated from other tissue and fixed directly in 4% formaldehyde in 1X PBS overnight at 4°C. To obtain cochlear epithelium, extraneous tissue and bone surrounding the cochlea were removed to obtain the cochlea duct. Reissner's membrane was removed to expose the sensory epithelium. The microdissected sensory epithelia were fixed in 4% formaldehyde containing 1X PBS overnight and washed with 1X PBS before being processed

for immunostaining and *in situ* hybridization. After processing, the cochlea, including spiral ganglion and sensory epithelium, was flat-mounted.

Immunohistochemistry

The micro-dissected cochlea tissues fixed in 4% formaldehyde in 1X PBS were permeabilized in wash buffer (1X PBS with 0.1% Triton X-100) for 10 min before incubated for at least 1 hour in blocking buffer (1X PBS with 0.1% Triton X-100 and 5% normal goat serum) at room temperature. Samples were incubated overnight at 4°C with appropriate primary antibodies diluted in the blocking solution. Samples were then washed 3X for 10 min 1X PBS and incubated with the appropriate combinations of DAPI (1 µg/ml), Alexa Fluor 488 (1:500 dilution), Alexa Fluor 568 (1:500 dilution) or Alexa Fluor 647 (1:500 dilution) conjugated secondary antibodies (Life Technologies) for 2 hours at room temperature and rinsed in wash buffer before mounting in Prolonged Gold Antifade (Life Technologies).

iMOP cells were fixed in 4% formaldehyde in 1X PBS for 20 minutes, permeabilized in wash buffer for 10 min, incubated in blocking buffer (1X PBS, 10% goat serum and 0.1% Triton X-100) for 1 hour and incubated overnight with the primary antibodies in blocking buffer. Cells were incubated with primary antibodies, rinsed in wash buffer and incubated with appropriate combinations of DAPI (1 µg/ml), Alexa Fluor 488, Alexa Fluor 568 or Alexa Fluor 647 conjugated secondary antibodies (Life Technologies) in blocking buffer for 2 hours. Samples were washed with 1X PBS and mounted in Prolonged Gold Antifade (Life Technologies). All antibodies are listed in Table 2.

Single-molecule *in situ* hybridization

Single-molecule fluorescence in situ hybridization (smFISH) was performed using RNAscope (Wang et al., 2012). The RNAscope multiplex fluorescent reagent kit version 2 (Advanced Cell Diagnostics) was used to detect target RNAs according to the manufacturer's instructions. RNAscope probes are listed in Table 3. Immunohistochemistry to enhance and detect tdTomato protein was performed after the smFISH

protocol. Samples were incubated in blocking buffer (1X PBS, 10% goat serum and 0.3% Triton X-100) for 1 hour at room temperature, followed by overnight incubation with rabbit anti-RFP (Rockland) in blocking buffer at 4°C. After incubation with primary antibodies, samples were washed with 1x PBS and incubated with appropriate combinations of DAPI (1 µg/ml) and Alexa Fluor 568 conjugated secondary antibodies (Life Technologies) in a blocking buffer for 2 hours at room temperature. Samples were washed with 1X PBS and mounted in Prolonged Gold Antifade (Life Technologies).

Fluorescence micrograph acquisition and visualization

Samples were mounted on a 1.5-cover glass and acquired on a Zeiss LSM800 point scanning confocal microscope. Antibody-conjugated fluorophores and tdTomato fluorescent protein were excited using four laser lines (405,488, 561, and 633nm). 1024X1024 images were acquired using either the 40X (1.4 NA) or 63X (1.4 NA) objective with 1.5-2x digital zoom and 4X Kalmann averaging. The brightness and contrast on images were adjusted and viewed using Zen Blue (Zeiss).

Cell Culture for iMOP cells

iMOP cells were grown in suspension with DMEM/F12 (Life Technologies) containing B27 supplement (Life Technologies), 25 µg/ml carbenicillin and 20 ng/ml bFGF (PeproTech). Cells were passaged weekly by dissociation with TrpLE Express (Life Technologies), harvested by centrifugation and resuspended in fresh medium. To generate iMOP-derived neurons, tissue culture dishes were coated with 10 µg/mL of poly-D-lysine for 1 hour aspirated and allowed to dry for 15 min, coated overnight with 10 µg/mL of laminin at 37°C, washed 3 times with 1X PBS before plating cells. Proliferating iMOP cultures were dissociated in TrypLE Express (Life Technologies), resuspended in neurobasal media and counted using a Moxi counter. Particles between 9-16 um were considered cells, and 1.5-2 $X10^4$ cells were seeded in a poly-D-lysine and laminin-coated well. The culture medium was switched to Neurobasal medium (Life Technologies) containing N21, 2 mM L-glutamine (Life Technologies), and 1 µM K03861 when the cells

were plated. Cultures were maintained in the medium for 7 days, and the medium was changed every other day before cells were harvested for immunostaining or CUT&Tag.

CUT&Tag

Cells from proliferating iMOPs and iMOP-derived neurons were harvested for and processed using the CUT&Tag-IT Assay Kit (Active Motif) described by the manufacturer. Cells were gently dissociated using TrpLE Express (Life Technologies), counted and collected by centrifugation. For each CUT&Tag reaction, 500,000 cells were used. The supernatant from the cell pellet was removed, and cells were resuspended in wash buffer and placed on ice. Cells were enriched using magnetic Concanavalin A beads and resuspended in an antibody buffer containing a primary antibody to the protein of interest. Antibodies for H3K4me3 (Active Motif), p300 (Developmental Studies Hybridoma Bank), CHD4 (Abcam) and IgG (Jackson Immunochemicals) were used for individual samples. All antibodies are listed in Table 2. Two independent samples were used for each antibody condition. Primary antibodies were incubated with the cells for 2 hours at room temperature to overnight at 4°C. All antibodies for CUT&Tag were used at 1:50 dilution. After incubation, the cells were washed and incubated in buffer containing the assembled pA-Tn5 transposomes and incubated for 1 hr at RT. Cells were washed and processed for tagmentation by incubation in the appropriate buffer for 1 hr at 37°C. A solution containing EDTA, SDS and proteinase K was added to stop the reaction and solubilize DNA fragments. The solution was placed on a magnetic stand, and the supernatant containing soluble DNA fragments was retained. The DNA solution was purified using a column. The DNA fragments were subjected to PCR amplification and purified using SPRI beads. Libraries generated were quantified and subjected to quality control before performing an Illumina Hiseq 3000 platform (2x150bp).

Peak calling

Paired-end CUT&Tag reads were aligned to mm10 genome assembly with bowtie2. Only mapped reads were retained, written to the output, and used for the downstream analysis (Langmead and Salzberg,

2012). The bowtie2 SAM output files were converted into BAM files using Samtools (Li et al., 2009). After alignment, sequence reads were scaled using the bamCoverage command in deepTools to remove duplicates and generate normalized bigwig files with reads as Reads Per Kilobase per Million (RPKM) (Ramirez et al., 2014). UCSC bigWigToBedGraph utility was used to generate bedgraph files from bigwig files (Kent et al., 2010). Peaks were called using Sparse Enrichment Analysis for CUT&RUN (SEACR) (Meers et al., 2019b). SEACR output bed files from CHD4, H3K4me3 and p300 were generated using CHD4, H3K4me3 and p300 bedgraph files as target files while using IgG bedgraph file as a threshold. BEDtools (Quinlan and Hall, 2010) was used to identify consensus peaks with at least 10% reciprocal overlap between replicate samples. Only consensus peaks were used for downstream analysis. CUT&Tag signal tracks were visualized on Integrative Genomic Viewer (IGV) (Robinson et al., 2011).

Identifying CHD4-bound promoters and enhancers

To perform a global survey of CHD4-bound promoters and enhancers, we first defined CHD4-bound promoters and enhancers in proliferating iMOPs and iMOP-derived neurons. H3K4me3 and p300 were used as promoter and enhancer marks, respectively. CHD4 bound promoters (CHD4+ H3K4me3+) and enhancers (CHD4+ p300+) in iMOPs were identified using bedtools intersect command. CHD4+ H3K4me3+ were identified as regions with at least one base pair overlap between CHD4 and H3K4me3 peaks. CHD4+ p300+ regions were defined using the same strategy using CHD4 and p300 peaks. SEACR total signals were obtained from the SEACR output file and plotted as box and whisker plots to show the quartiles, mean (circle) and median (line) values. Cell state-specific CHD4-bound promoters or enhancers were identified based on their presence or absence in progenitors and neurons. Genome arithmetic was done using bedtools.

Heatmap and profile plots

Heatmaps and profile plots were generated using deepTools. The signal and region files were obtained from CUT&Tag data. Normalized bigwig files from two replicates were merged using bigwigCompare to

acquire average bigwig files and used as signal files. The summit regions corresponding to the maximum SEACR peak signal from CHD4 were used as region files. To visualize CHD4 and H3K4me3 reads as heatmaps or profile plots, deepTools were used. Plots were centered at summits of CHD4+ H3K4me3+, and the average CHD4 or H3K4me3 bigwig signals were plotted +/- 3 kb from the summits. To visualize CHD4 and p300 reads, the summits from CHD4+ p300+ were used as the center, and the average bigwig signals of either CHD4 or p300 bigwig files were plotted within +/- 3kb of the summits.

Quantification of heatmap total signals

To quantify CUT&Tag signals displayed in heatmaps, deepTools the --outFileNameMatrix option was used to retrieve the matrix of signal values underlying the heatmaps. CUT&Tag signals within specified genomic regions were added to obtain the summed signal values. Heatmap signals between progenitors and neurons within the +/- 3kb window were visualized as box and whisker plots.

Gene ontology (GO) analysis

To annotate CHD4+ common and neuron-specific promoters and enhancers, ChIPpeakAnno was utilized to determine the closest genes along with the corresponding ensembl gene IDs to those regions (Zhu et al., 2010). Unique ensembl gene IDs near CHD4-bound promoters and enhancers were used for GO analysis using DAVID (The Database for Annotation, Visualization and Integrated Discovery) (Huang et al., 2009).

Statistical analysis

Statistical analyses were performed using either R or OriginPro (Origin Lab) for normally distributed data. The means of data were presented and subjected to an unpaired two-tailed Student's t-test to determine statistical significance and provide a p value. Results with p values <0.05 were considered statistically significant. Unless noted, the p values are defined as $*p<0.05$, $**p<0.01$, and $***p<0.001$. Bar graphs

display the means ± standard error of the mean (SEM), and violin plots show the distribution and mean of the data points.

Data for CUT&Tag and RNAscope were determined not to be normally distributed using the Shapiro-Wilks normality test. The median was presented and subjected to a non-parametric Wilcoxon rank-sum test to determine whether the paired samples differed statistically. Analysis of the data was performed in R. The normalized read counts (RPKM) from CUT&Tag were displayed as box and whisker plots to show the quartiles, means and medians. Horizontal lines within the box denoted the median values, while the circles represented the means. The number displayed in the text indicates the median ± standard deviation of CUT&Tag signals for box and whisker plots. The RNAscope images were counted to determine the distribution, mean and median of puncta counts per cell. Unless noted, the p values from the Wilcoxon rank-sum test were defined as $p < 0.0001$ to be significant. The variance was calculated as the sum of the squared difference between puncta counts and the sample mean and divided by the sample size minus one. The Levene test for the homogeneity of variance was used to determine whether the variances were statistically significant. The p values from the Levene test were defined as $p<0.05$ to be significant.

Results

CHD4 expression in cochlear cell types

SGNs are bipolar and pseudounipolar neurons of the cochlea. The soma of SGNs reside within the modiolus and extends a peripheral process through Rosenthal's canal towards the sensory hair cells, while a central process from the cell soma projects to the cochlear nucleus in the brainstem. SGNs are broadly classified as type I and type II neurons. Type I SGNs are the primary afferents that consist of 90-95% of the neuronal population in the spiral ganglion. Type I SGNs are myelinated and form a single synaptic bouton with inner hair cells that reside in the organ of Corti (Fig. 1A). Multiple type I SGNs synapse along the basolateral surface of inner hair cells (IHCs) (Liberman, 1982). Type I SGNs differ in sensitivity to sound and spontaneous firing rate (SR), as revealed by single-fiber recordings in the cat auditory nerve (Kiang et al., 1965). The relationship between threshold and SR predicted three distinct populations of low, medium and high SR neurons (Liberman, 1978). These three subtypes are present irrespective of tonotopic position along the length of the cochlea (Borg et al., 1988; el Barbary, 1991; Schmiedt, 1989; Shrestha et al., 2018; Sun et al., 2022; Taberner and Liberman, 2005; Winter et al., 1990). SGNs display different receptors and ion channel regulators that shape their sensitivity and SR. The molecular heterogeneity has been correlated to the differences in electrophysiological properties of these neurons (Adamson et al., 2002; Chen et al., 2011; Liu et al., 2014; Liu and Davis, 2014).

Type II afferent neurons account for 5–10% of the neuronal population (Ruggero et al., 1982; Spoendlin, 1972). Type II SGNs are pseudounipolar and unmyelinated neurons that turn towards the cochlear base (Zhang and Coate, 2017). During outgrowth, Type II SGN peripheral axons turn after the growth cone passes between the basolateral surfaces of the inner pillar cells. Turning occurs among the outer pillar and Deiters' cells as they are directed towards the cochlear base (Fig. 1A). This process is mediated by planar cell polarity complexes formed between cochlear-supporting cells for non-cell autonomous

regulation of axon pathfinding (Ghimire and Deans, 2019; Ghimire et al., 2018). The peripheral axons then gradually ascend apically toward the outer hair cells (OHCs) after turning to join other type II axons in one of three outer spiral bundles that extend along the length of the cochlea (Fig. 1B). Each type II afferent neuron innervates multiple OHCs from the same row, with individual OHC receiving an *en-passant* contact from a type II afferent neuron (Zhang and Coate, 2017).

To determine the expression of CHD4, neonatal cochleae from embryonic (E)18.5 embryos were harvested. At this point, type I and type II SGNs are morphologically distinct, and the neurites have extended toward IHCs and OHCs, respectively. The cochleae were subjected to immunostaining with CHD4 and TUBB3 antibodies to mark the presence of type I and type II SGNs along with CHD4 (Fig. 1C). The fiber tracks from their innervation pattern can identify the type of SGNs. As previously described, many different cell types within the organ of Corti, including IHCs and OHCs, express CHD4 (Layman et al., 2013). We confirmed the presence of CHD4 in MYO7A labeled hair cells (Fig. 1D). CHD4 was also expressed in the nuclei of inner pillar, outer pillar and the three rows of Dieter cells and other supporting cells (Fig. 1E). Finally, CHD4 was strongly expressed in the nucleus of spiral ganglion neurons (SGNs) marked by TUBB3 in the modiolus (Fig. 1F). Expression of CHD4 was present in all TUBB3-marked SGNs. The presence of *Chd4* transcripts in developing SGNs (Lu et al., 2011) and our results suggest that CHD4 may function in SGNs during inner ear development.

Deletion of *Chd4* in SGNs

CHD4 is present in many inner ear cell types, and mutations that inactivate CHD4 chromatin remodeling activity may contribute to improper development or dysfunction of multiple inner ear cell types. Since SGNs were highly expressed CHD4, we wanted to delineate how CHD4 ablation in SGNs contributes to the development of the cochlea and hearing loss. Targeted ablation of CHD4 from SGNs using a Neurogenin1 (Ngn1) CreER^{T2} *Chd4*$^{flox/flox}$ animal was accomplished. The Ngn1 CreER^{T2} *Chd4*$^{flox/flox}$

282 animals contain two copies of the *Chd4* conditional knockout (cKO) allele where loxP sites flanked exons
283 that code for the ATPase domain required for nucleosome repositioning (Williams et al., 2004). The Ngn1
284 CreER^{T2} transgenes harbor a tamoxifen-inducible Cre expressed in neurosensory progenitors and can
285 be used for genetic manipulations in SGNs (Koundakjian et al., 2007). Tamoxifen administration to Ngn1
286 CreER^{T2} animals allowed Cre-mediated excision of loxP-flanked DNA in inner ear neurosensory
287 progenitors that become SGNs (Koundakjian et al., 2007; Raft et al., 2007). To ensure Cre activity was
288 present in the intended cell types, *Chd4*$^{flox/flox}$ Ngn1 CreER^{T2} were crossed to the Ai9 tdTomato reporter
289 (Madisen et al., 2010). In the triple transgenic animals, tamoxifen administration allows Cre-activated Ai9
290 tdTomato reporter expression and enables fluorescence visualization of SGN cell bodies and axonal
291 projections while simultaneously deleting *Chd4* (Fig. 2A). Control (Ngn1 CreER^{T2}; Ai9) and *Chd4* cKO
292 (Ngn1 CreER^{T2}; *Chd4*$^{flox/flox}$; Ai9) lines were generated. Timed matings from either control or *Chd4* cKO
293 lines produced pregnant dams were administered with tamoxifen to produce embryos for analysis.
294
295 During inner ear development, delaminating otic progenitors around embryonic day (E)9 from the
296 proneurosensory domain of the otic vesicle coalesce to form the cochlear-vestibular ganglion (CVG). As
297 development progresses, the CVG neurons segregate to create the spiral ganglion. A population of
298 neurons exits the cell cycle and terminally differentiates at the base and middle of the cochlea starting
299 from E9.5-10.5. Most SGNs exit the cell cycle around E11.5 in the middle and base of the cochlea, while
300 cells in the apex exit the cell cycle at E12.5. After exiting the cell cycle, peripheral projections from SGNs
301 extend toward the sensory epithelium of the cochlea. At E12.5, SGN projections begin to extend beyond
302 the spiral ganglion border. At E15.5, SGN peripheral axon outgrowth continues along the length of the
303 cochlea. Type I SGNs form radial fiber bundles that undergo fasciculation. Between E15.5-18.5, type I-
304 like SGN processes show extensive branching around and beyond the inner hair cells. The neurites are
305 subsequently refined by retracting from the outer hair cell region (Appler and Goodrich, 2011; Coate et
306 al., 2015). Type II SGNs are notably distinct from Type I SGNs by E16.5 based on their peripheral
307 projections ending at the outer hair cell region (Bruce et al., 1997). The Ngn1 CreER^{T2} animals with a

reporter can mark delaminating neurosensory progenitors that develop into type I and type II SGNs at the aforementioned developmental stages (Koundakjian et al., 2007).

Chd4 was deleted by administering daily tamoxifen doses to pregnant dams between E8.5-10.5. During this time, *Chd4* was deleted from neurosensory progenitors that give rise to SGNs. Labeled cells were used to study the consequences of *Chd4* ablation in the development of type I and type II SGNs. E18.5 embryos were harvested from pregnant dams after tamoxifen treatment. Although some embryos survived, many resorptions occurred perinatally after tamoxifen administration. Quantification and comparison of resorbed embryos from control and *Chd4* cKO dams suggest a significant reduction in viability of *Chd4* cKO embryos (Fig. S1A). Quantifying the number of surviving embryos from individual litters obtained from pregnant dams showed a statistically significant reduction in embryo viability after *Chd4* deletion (Fig. S1B). Cre recombinase expression in the Ngn1 CreERT^2 is not limited to the inner ear but can also be observed throughout the central nervous system (Kim et al., 2011). These findings suggest that deleting *Chd4* in other cell types may decrease viability in the *Chd4* cKO embryos.

From the remaining embryos, cochleae were harvested and used for immunostaining. To ensure that genetic deletion of *Chd4* lacked protein, immunofluorescence labeling of the CHD4 protein was done. TUBB3 immunofluorescence was used to identify SGNs. The tdTomato fluorescence suggested Cre activity was present in TUBB3 marked SGNs in both control and *Chd4* cKO cochleae samples. Even though SGNs were present in the cochleae, only the CHD4 signal was seen in controls and not *Chd4* cKO cochleae (Fig. 2B). These results showed that CHD4 protein was absent in the *Chd4* cKO cochlea after tamoxifen treatment and that CHD4 was not essential for SGN viability at embryonic and neonatal stages. In E18.5 embryonic cochlea, an increase in the number of tdTomato+ and TUBB3-negative cells was observed in *Chd4* cKO (Fig. 2C). To quantify the percentage of the marked cell populations, SGNs from dissected cochlea were divided into three regions corresponding to the apex, middle and base of the cochleae. In controls, a low percentage of cells lacking TUBB3 but expressing tdTomato was

observed (apex: 6.81 ± 1.69%, middle: 4.07 ± 1.94%, base: 3.95 ± 1.74%), while in *Chd4* cKO cochlea, increased percentages of these cells were observed along the length of the cochleae (apex: 12.06 ± 2.25%, middle: 8.73 ± 0.91%, base: 7.82 ± 1.29%; apex, $p<0.136$, middle, $p<0.095$; base, $p<0.148$) (Fig. 2D). The percentage of TUBB3 labeled SGNs marked by tdTomato allowed us to confirm the efficiency of Cre-mediated activity in these cells. In control embryos, Cre activity was observed in almost all SGNs with a slight decrease in labeled cells at the apex (apex: 89.86 ± 3.56%, middle: 97.09 ± 1.48%, base: 98.97 ± 0.36%). Since development proceeds in a base-to-apex manner, the decreased percentage of tdTomato-marked cells located at the apical region of the cochlea was likely due to a small population of late-born neurons that was not exposed to tamoxifen during the time window of administration. *Chd4* cKO displayed similar percentages of tdTomato marked cells (apex: 84.35 ± 2.99%, middle: 95.71 ± 1.96%, base: 98.91 ± 0.2%; apex $p<0.302$; middle $p<0.603$; base, $p<0.9$). The percentages of tdTomato+TUBB3+ cells from control and *Chd4* cKO cochlea were not statistically different (Fig. 2E). The numbers of tdTomato+ cells from *Chd4* cKO were not significantly different from control (44.22 ± 0.41% for control, 49.7 ± 2.32% for *Chd4* cKO, $p<0.081$) (Fig. 2F). These results suggest that tamoxifen-induced Cre recombination was efficient along the entire length of the cochlea and was similar between control and *Chd4* cKO cochleae.

Chd4 cKO cochleae displayed altered fasciculation of radial fiber bundles

Deletion of *Chd4* in embryos showed that SGNs were present and in comparable percentages as controls. Although *Chd4* may not dramatically affect the viability or early developmental stages, we wanted to determine whether loss of *Chd4* showed discernable differences at later stages. Post-mitotic neurons from the spiral ganglion extend neurites towards inner and outer hair cells, starting from the base to the apex. Type I and type II SGNs target IHCs and OHCs, respectively. Type I and type II SGN fiber tracks and innervation patterns were marked by performing whole mount TUBB3 immunostaining using cochleae from control and *Chd4* cKO (Fig 3A).

The peripheral axons of type I SGNs extend from the soma to form a radial bundle. The type I SGN fibers fasciculate, the terminals extensively branch around the inner spiral plexus (ISP) and retract from the outer hair cell region back into the IHC region (Fig 3B). In *Chd4* cKO cochleae, radial fibers were less compact and showed wider nerve fascicles. The area between the fiber bundles was identified by converting TUBB3 immunofluorescent images to black-and-white binary images. The white regions between fiber bundles and the total area from the SGN soma to the sensory epithelium were determined from images taken along the length of the cochlea (Fig. 3C). The percent area unoccupied by radial fibers relative to the total area was calculated, and used as a metric for fasciculation (Fig. 3D). The average percentage of unoccupied space in *Chd4* cKO cochleae was significantly decreased (33.19 ± 2.59% for control and 25.12 ± 1.28% for *Chd4* cKO, $p<0.049$). The result suggested that the radial fibers from *Chd4* cKO cochleae covered more area and thus were wider than controls (Fig. 3E). The fiber bundles were counted in control and *Chd4* cKO cochleae to determine the fascicle numbers in the inner spiral plexus (ISP), (Fig. 3F). The ISP consists of the region where radial fibers extend from the soma through the *habenula perforata* to innervate the IHC (Fig. 1). The average number of fascicles in ISP per inner radial bundle increased significantly in *Chd4* cKO cochleae (4.48 ± 0.16 bundles for control and 6.54 ± 0.67 bundles for *Chd4* cKO, $p<0.0083$) (Fig. 3G). These results show an increased number of inner radial fiber bundles and less compact bundling of the nerve fiber.

Chd4 cKO cochleae display improper turning of type II fibers

Type II SGNs constitute only 5-10% of the total SGN population, but their axonal projections are spatially distinct from type I SGNs. During development, their peripheral processes cross the tunnel of Corti into the outer hair cell region, where the axons make a right-angle turn and travel from the base of the cochlea towards the apex to make *en passant* synapses with outer hair cells. The outer spiral fibers are the bundled neurites from type II SGNs that extend along the OHC region. Each OHC is innervated by 2-5

type II SGNs (Huang et al., 2012; Martinez-Monedero et al., 2016). To look at the outer spiral fiber tracks, TUBB3 labeled neurons from whole mount cochleae were used for analysis (Fig. 4A). The magnified images of outer spiral fibers usually display three main fiber tracks that travel along individual rows of outer hair cells with intermittent fibers crossing these tracks. To show quantitative differences between the outer spiral tracks, intensity profiles from control and *Chd4* cKO cochleae images spanning the outer hair cell region were taken (Fig. 4B). Measurements of the intensity profile show different peaks corresponding to the presence of fibers. The intensity profile plot showed three prominent peaks in the control cochlea (black). In contrast, Chd4 cKO cochlea (red) displayed additional peaks (Fig. 4C). The data suggested that there are type II SGN fibers or individual axons that detract from the outer fiber tracts (Fig. 4C). Each major peak corresponds to an outer spiral bundle consisting of multiple fibers. The appearance of the minor peaks within a major peak corresponds to the increased dispersion of the fibers within an outer spiral fiber. The number of distinct fibers observed by fluorescent microscopy in the outer hair cell region was counted and normalized based on the area to validate the altered axon paths. Similar to the intensity profile, the number of fibers in the OHC area increased in *Chd4* cKO samples compared to controls (13.98 ± 0.73 fibers for control and 17.64 ± 0.78 fibers for *Chd4* cKO, $p<0.027$) (Fig. 4D). These results suggest aberrant bundling of the outer spiral fibers after *Chd4* ablation in SGNs.

We also noticed the aberrant turning of the outer spiral fiber tracks. Turning of the type II SGN fibers usually occurs near the inner pillar cell (IPC), outer pillar cell (OPC) or Dieter cell (DC) region. Confocal micrographs were acquired below the outer hair cell layer up to the sensory epithelium to visualize the fiber turning. Individual fibers from control cochleae turned towards the base of the cochlea before joining one of the three outer spiral fiber tracks. In contrast, the *Chd4* cKO cochleae showed fibers turning in the opposite direction (Fig. 4E, yellow arrows). Incorrectly turned type II fibers were quantified in control and Chd4 cKO cochleae (Fig 4F). These data showed that the deletion of *Chd4* increases the incorrect turning of type II SGNs in the outer spiral fibers (0.12 ± 0.06 fibers for control and 1.93 ± 0.14 fibers for *Chd4* cKO, $p<0.00028$. Turning of the fibers has previously been shown to require cell signals from supporting

cells (Deans, 2022; Ghimire and Deans, 2019; Ghimire et al., 2018). To ensure that supporting cells in the organ of Corti were present and not indirectly affected by *Chd4* deletion, immunostaining for both hair cells using MYO7A and supporting cells SOX2 was performed in control and Chd4 cKO cochlea. A single row of inner hair cells and three rows of outer hair cells were present in both samples. Moreover, SOX2-labeled supporting cells showed the presence of organized supporting cells residing below hair cells (Fig. S2). These results suggest that *Chd4* deletion in SGNs affects the turning of type II SGNs in a cell-autonomous manner.

Chd4 cKO cochleae display aberrant basal to apical axon path towards outer hair cells

Alterations in axon paths could also be due to how fibers exit Rosenthal's canal and ascend toward the outer hair cells. To determine if this is the case, reconstructed confocal images of MYO7A-labeled hair cells provide a landmark for the terminal destination of axons. We observed that many type II tracks take a more circuitous route toward the OHCs because the fibers initially descend basally and migrate further away from the soma of outer hair cells (Fig. 4G). The distances were obtained from the bottom of individual OHC somas to the furthest detectable axon fibers directly below. The measurements were used to quantify the aberrant axon path (Figure 4H). The measurements showed an increase in the average distance of the fibers to the bottom of hair cells in *Chd4* cKO cochleae (17.84 ± 0.66μm for control and 29.87 ± 3.74μm for *Chd4* cKO, $p<0.034$). The increased distance measured in *Chd4* cKO cochleae suggested that outer spiral fibers do not properly ascend from Rosenthal's canal towards the outer hair cells (Fig. 4I). Many of these changes in fiber tracks and innervation patterns observed both in type I and type II SGNs are reminiscent of axon guidance defects. Although these findings implicate CHD4 in axon pathfinding, the molecular targets for CHD4 in SGNs are unknown.

Enrichment of CHD4 at cis-regulatory regions of _Eph_ and _Ephrin_ genes

CHD4 function is cell-type dependent, and its chromatin activity likely alters a unique repertoire of cis-regulatory elements in SGNs to control gene expression. A significant hurdle is identifying high-confidence occupancy sites for CHD4 in SGNs by chromatin immunoprecipitation followed by deep sequencing (ChIP-seq) or Cleavage Under Targets & Tagmentation (CUT&Tag). The inability to identify these high-confidence sites in SGNs is partly due to the large number of cells required for the experiments. Instead of primary SGNs, we used immortalized multipotent otic progenitor (iMOP)-derived neurons to determine genome-wide binding sites for CHD4 to identify potential target genes. Immortalized multipotent otic progenitors (iMOP) derived neurons are highly similar at the transcriptome level to primary otic progenitors from which they were derived and can differentiate into cells that display bipolar and pseudounipolar morphology similar to SGNs (Kwan et al., 2015).

Immunostaining confirmed the presence of CHD4 in the nucleus of proliferating iMOPs and TUBB3-expressing iMOP-derived neurons (Fig. 5A). To identify genome-wide CHD4 binding sites, CUT&Tag was performed using CHD4 antibodies on proliferating iMOP and iMOP-derived neurons. CHD4 occupancy is cell-type specific and are recruited to active promoters and enhancers to repress transcription (Yang et al., 2016; Yoshida et al., 2019). We used the H3K4me3 and p300 marks as genomic landmarks for promoters and enhancers. Sparse Enrichment Analysis for CUT&RUN (SEACR) identified regions of high-confidence enrichment, known as peaks, from all CUT&Tag sequence reads (Meers et al., 2019a). We compared CHD4 peaks to H3K4me3 and p300 bound regions. The heatmaps provided a distribution of the reads within a +/- 3 kb window. The profile plots allowed us to evaluate the read density over the same genomic regions qualitatively. We identified CHD4+ H3K4me3+ regions based on the occupancy of CHD4 and H3K4me3 peaks in proliferating iMOP cells and iMOP-derived neurons (Fig. S3B). The CHD4+ H3K4me3+ regions corresponded to CHD4-bound promoters. Similarly, we defined CHD4+ p300+ regions in proliferating iMOP cells and iMOP-derived neurons (Fig. S3C). The CHD4+ p300+ regions corresponded to CHD4-bound enhancers. From the profile plots, we noticed that the CHD4 signal increased in iMOP-derived neurons compared to proliferating iMOPs at both promoters

and enhancers. We quantified and compared the CHD4 total signals at CHD4+ H3K4me3+ promoters and CHD4+ p300+ enhancers between proliferating iMOP and iMOP-derived neurons. We showed that at CHD4-bound promoters, CHD4 total signals increased 2.80 fold in iMOP-derived neurons (57,811.40 ± 65,983.40 RPKM) compared to proliferating iMOPs (20,684.90 ± 25,408.89 RPKM, $p<2.2 \times 10^{-16}$). At CHD4-bound enhancers, we found a 4.65 fold increase of CHD4 total signals in iMOP-derived neurons (134,027.50 ± 102,349.97 RPKM) compared to proliferating iMOPs (28,837.65 ± 29,014.11 RPKM, $p<2.2 \times 10^{-16}$) (Fig. 5B). The results suggest that increased enrichment of CHD4 at cis-regulatory regions in iMOP-derived may regulate gene expression during neuronal differentiation.

To investigate the involvement of CHD4 during neuronal differentiation, we identified CHD4 binding sites present in iMOP-derived neurons. We did this by comparing CHD4-bound regions between proliferating iMOPs and iMOP-derived neurons. At CHD4+ H3K4me3+ promoters, we found 982 progenitor-specific, 168 neuron-specific, and 1,092 common promoters in both proliferating iMOPs and iMOP-derived neurons. At CHD4+ p300+ enhancers, we identified 2,106 progenitor-specific, 223 neuron-specific, and 750 common enhancers (Fig. 5C). We focused on common and neuron-specific regions since CHD4 activity may exert epigenetic changes at these sites during neuronal differentiation. We generated heatmaps and profile plots for each of the regions. At common promoters, we observed a 1.20-fold increase of H3K4me3 in iMOP-derived neurons (25,871.92 ± 12,797.1 RPKM) compared to proliferating iMOPs (21,550.36 ± 9,015.1 RPKM, $p<3.67 \times 10^{-23}$) and a 2.28-fold increase in CHD4 in iMOP-derived neurons (5,407.49 ± 2,955.04 RPKM) compared to proliferating iMOPs (2,371.49 ± 1573.27 RPKM, $p<3.46 \times 10^{-282}$). At neuron-specific promoters, a 1.3 fold increase in H3K4me3 (proliferating iMOP 17,105.85 ± 10,709.21 RPKM, iMOP-derived neurons 22,411.04 ± 14,180.57 RPKM, $p<3.87 \times 10^{-7}$) and 3.30 increase in CHD4 (proliferating iMOP 1,397.09 ± 2,617.01 RPKM, iMOP-derived neuron 4,608.37 ± 3,173.27 RPKM, $p<4.22 \times 10^{-45}$) was observed in iMOP-derived neurons (Fig. 5D). All observed increase in H3K4me3 and CHD4 were statistically significant.

We performed a similar analysis for enhancers. The heatmaps and profile plots showed a distribution of p300 and CHD4 centered at common and neuron-specific enhancers. A 3.37-fold increase in p300 (proliferating iMOP = 2,838.41 ± 1,713.93 RPKM, iMOP-derived neuron = 9,578.39 ± 4531.32 RPKM, $p<5.92 X10^{-223}$) was observed at common enhancers. CHD4 displayed a 2.84-fold increase in signal from iMOP-derived neurons (proliferating iMOP 4,068.79 ± 2,542.82 RPKM, iMOP-derived neuron 11,559.34 ± 4,647.43 RPKM, $p<9.30 X10^{-210}$). At common and neuron-specific enhancers, a statistically significant increase in signal was detected for p300 and CHD4 in iMOP-derived neurons compared to proliferating iMOPs (Fig. 5E). These results suggest that CHD4 was significantly enriched at specific promoters and enhancers during neuronal differentiation. The increased occupancy likely alters the chromatin state of these cis-regulatory regions to modulate transcription.

To gain biological insights into CHD4 targets, genes near the common and neuron-specific regulatory elements were identified (Table S1). The identified target genes were used for gene ontology analysis. Gene ontology (GO) analysis revealed function in chromatin organization ($p< 5.1X10^{-14}$), which is consistent with the predicted cellular process of CHD4 in inner ear neurons. Other biological processes such as ephrin receptor signaling ($p< 4.9X10^{-5}$), axon guidance ($p< 2X10^{-13}$), semaphorin-plexin signaling during axon guidance ($p< 2.7X10^{-2}$), axonal fasciculation ($p< 1.6X10^{-2}$), and axonogenesis ($p<1.6X10^{-14}$) were some of the notable cellular processes (Fig. S3A). The GO analysis suggested that CHD4 gene targets may regulate processes involved in axon pathfinding, including ephrin receptor signaling. We identified *Epha4*, *Epha7*, *Ephb3*, *Efna3*, *Efna4*, *Efnb2*, *Efna5*, *Efnb1*, and *Ephb2* as candidate genes involved in ephrin receptor signaling based on their proximity to CHD4-bound promoter and enhancer regions (Table S1). Ephrin signaling pathways are essential in guiding SGN peripheral axons. We focused on *Epha4*, *Epha7*, and *Efnb2* because these genes have previously been implicated to function in the inner ear (Coate et al., 2012; Defourny et al., 2013; Kim et al., 2016; Petitpre et al., 2018; Sanders and Kelley, 2022). At *Epha4* and *Epha7*, CHD4 and H3K4me3 peaks were observed near the transcriptional start site. We also observed an increase in CHD4 and p300 in iMOP-derived neurons at

multiple intronic regions, a region upstream at *Epha4* and a singular downstream site at *Epha7* (Fig. 5F). A similar observation was noted for *Efnb2* (Fig. S3D), where CHD4 was enriched at the H3K4me3 marked promoter along with increased CHD4 and p300 signals at a downstream enhancer region. These results implicate that CHD4 binding to promoters and enhancers may control the transcription of ephrin receptors and ligands. The altered expression of these genes may be pertinent to the axon guidance deficits seen in the *Chd4* cKO cochleae.

Chd4 cKO showed increased *Epha4* mRNA levels in SGNs

To test if deletion of CHD4 in SGNs affects the level of ephrin molecules, cochleae from control and *Chd4* cKO were subjected to RNAscope fluorescence *in situ* hybridization. We used *Epha4*, as an example of how transcription is affected after CHD4 ablation. *Calbindin2* (*Calb2)* transcripts were used as a marker for SGNs. TUBB3 immunolabeling was combined with RNAscope to demarcate individual cells for quantification (Fig. 6A). The number of counted punctas from RNAscope measured the relative number of mRNA molecules. *Calb2* and *Epha4* puncta were counted from individual TUBB3 marked SGNs. The average number of *Epha4* puncta in the SGN population increased significantly in *Chd4* cKO (13 ± 6.29 *Epha4* puncta/cell) compared to control (7 ± 4 *Epha4* puncta/cell, $p<2.2 \times 10^{-16}$) and was statistically significant. Concurrently, there was no significant difference observed in *Calb2* transcript levels between *Chd4* cKO (8 ± 5.51 Calb2 puncta/cell) and control (9 ± 6.16 *Calb2* puncta/cell, p<0.13) (Fig. 6B). The distribution of puncta counts per cell was visualized by plotting the *Calb2* and *Epha4* puncta counts separately (Fig. 6C) In addition to the increase in puncta counts for each cell in *Chd4* cKO SGNs, we noted an increased variance of *Epha4* counts per cell. The variance provides the spread of puncta per cell around the median. Each histogram was converted to a kernel density estimate to describe the distribution probability of puncta in cells. A 2.47-fold increase in the variance of *Epha4* transcripts was observed in *Chd4* cKO (σ^2 = 39.5) compared to control SGNs (σ^2 = 15.99, $p<2.27 \times 10^{-14}$). The non-overlapping regions in the kernel density estimates reflect the increased probability of observing cells

with higher *Epha4* transcript levels in the absence of *Chd4* (Fig. 6D). In contrast, the variance of *Calb2* transcripts showed a 1.25-fold decrease in *Chd4* cKO (σ^2 = 30.36) compared to the control (σ^2 = 37.93, p <0.035). Although the variance for *Calb2* is significant, we did not observe CHD4 or the H3K4me3 mark at the *Calb2* promoter (Fig. S3E). The enrichment pattern at *Calb2* was distinct from *Epha4*, *Epha7,* and *Efnb2*, suggesting an indirect effect of *Chd4* deletion or a different mechanism causing the decreased variance. The results suggest that the increased likelihood of *Chd4* cKO SGNs to harbor more *Epha4* transcripts is likely due to the loss of transcriptional repression. The data indicate that CHD4 normally fine-tunes transcription in SGNs during development, and ablation of *Chd4* increases transcript levels of axon guidance genes, resulting in aberrant peripheral axon pathfinding.

Discussion

De novo pathogenic variants of *CHD4* correlate to SIHIWES, an autosomal dominant neurodevelopmental disorder**.** Patients with pathogenic variants of CHD4 show variable symptoms, and many display hearing loss (Sifrim et al., 2016b; Weiss et al., 2016). CHD4 is expressed in cochlear supporting cells and hair cells from E18 to P21 (Layman et al., 2013). Gene expression analysis showed that CHD4 transcripts are present and changing in developing murine SGNs from E12 to P15 (Lu et al., 2011). CHD4 has a core ATPase SWI/SNF domain that hydrolyzes ATP and converts it into chromatin repositioning activity. Some pathogenic mutations result in a CHD4 protein with reduced chromatin remodeling activity (Weiss et al., 2020). To clarify the contribution of CHD4 in SGNs, we employed a conditional knockout mouse model that allows Cre-dependent inducible deletion of the exons coding for the ATPase domain of CHD4 in SGNs. The conditional knockout mouse allowed us to separate the CHD4 function from other inner ear cell types, such as hair cells and supporting cells. Our current results implicate a cell-autonomous role for CHD4 in the pathfinding of SGN peripheral axons during inner ear development. The lack of CHD4 chromatin remodeling activity in SGNs may result in aberrant axon guidance. The altered pathfinding may affect the transmission of neural signals and innervation of hair

cells. These deficits likely contribute to hearing loss in patients with SIHIWES and provide insight into how other neural circuits may be affected.

CHD4 is a core subunit in the Nucleosome Remodeling and Deacetylase (NuRD) complex (Tong et al., 1998; Xue et al., 1998; Zhang et al., 1998). The NuRD complex acts mainly as a transcriptional repressor and localizes to sites of active transcription. At these sites, CHD4 repositions nucleosomes and subunits of the complex, such as histone deacetylases (HDAC) 1 and 2 deacetylate histones (Morra et al., 2012; Watson et al., 2012). Although CHD4 has many other paralogs, distinct NuRD complexes with individual CHD paralogs (CHD3, CHD4, and CHD5) have specific molecular functions and do not compensate for the loss of a singular CHD. The remaining paralogous CHDs did not compensate for the cellular effects of ablating CHD4 (Nitarska et al., 2016). CHD4-containing NuRD complexes in the inner ear may contain distinct protein subunits that alter the epigenetic landscape at cis-regulatory regions. Our results suggest a role for CHD4 in axon guidance during SGN development. Even if paralogs were present in SGNs, they did not fully compensate for the observed axon guidance deficits. We used iMOP-derived neurons as a cellular system to show CHD4 occupancy at distinct sets of promoter and distal enhancers. During iMOP neuronal differentiation, we observed increased CHD4 occupancy at these sites. We propose that CHD4 exerts epigenetic changes on cis-regulatory elements to attenuate transcription of axon guidance genes until the appropriate developmental time. In the absence of CHD4, the core NuRD complex does not form, and axon guidance genes may show increased transcription due to the absence of NuRD-dependent nucleosome repositioning and histone deacetylase activities. The exquisite temporal transcriptional control of axon guidance genes is likely required for appropriate fasciculation and innervation patterns.

Our identified candidate set of Eph receptors and Ephrin ligands (*EphA4*, *EphA7*, and *Efnb2*) is noteworthy since their functions are well-established in the developing cochlea. *Eph* receptors are a family of receptor tyrosine kinases that mediate many essential processes through promiscuous

interactions with membrane-bound ephrin ligands. Ephrins are divided into the glycosyl-phosphatidylinositol (GPI) linked ephrin-A and the transmembrane ephrin-b ligands. Ephrins bind to Eph receptors of the same class, except for EphA4. EphA4 interacts with ephrin-A, B2, and B3 ligands.

Deletion of *EphA4* showed ectopic innervation of outer hair cells by a subset of type I SGNs (Defourny et al., 2013). EphA4 interacts with the ephrin-A5 ligand to control target specification, expressed primarily in OHCs and a subset of type I SGNs. Previously, *ephrin-A5* was thought to be expressed in a subset of type I SGNs, but recent evidence implicated *ephrin-A5* mainly in type II SGNs (Petitpre et al., 2018; Sanders and Kelley, 2022). The otic mesenchyme surrounding the SGN axons also expresses EphA4 (Coate et al., 2015). This pattern of EphA4 expression guides fasciculation through ephrin-B2 interactions on the developing SGN axons. Another Eph receptor, EphA7, in SGNs, is required for neurite outgrowth. Loss of *EphA7* resulted in more sparse fiber bundles and fewer synaptic contacts on inner hair cells (Kim et al., 2016). These studies implicate the function of ephrin signaling in developing peripheral auditory circuits. Although we observed axon guidance deficits in the *Chd4* cKO cochleae, the phenotypes are distinct. Using the Ngn1 CreER^{T2}, we only perturbed SGNs while leaving the other cell types, such as hair cells and otic mesenchyme, untouched. Instead of inactivating the function of ephrin receptor or ephrin ligands, *Chd4* deletion increased *Epha4* transcript levels in SGNs, revealing a molecular perturbation relevant to SIHWES disease. The *Chd4* cKO model also differs from the Eph receptor and Ephrin ligand single knockouts because it likely affects the expression of multiple axon guidance genes. The subtle cellular phenotypes in single Eph and Ephrin knockout mice suggest that the proper wiring of the peripheral auditory circuit may require the combined effects of multiple Eph and Ephrins members instead of relying on a single molecule. Our findings align with the function of numerous Eph and ephrin genes during SGN development and suggest that CHD4 may coordinate the expression of several Ephrin ligands and receptors to shape the innervation pattern of type I and II SGNs.

Control of gene expression plays a fundamental role in development and disease. Patients with Sifrim-Hitz-Weiss disease show variable congenital disabilities. This observation is reminiscent of CHARGE syndrome, a genetic disorder caused by pathogenic variants in CHD7. CHD7 and CHD4 are part of the chromodomain helicase DNA-binding protein family (Micucci et al., 2015). Global chromatin regulators such as CHD7 and CHD4 can robustly affect transcription and trigger cell-autonomous changes during critical periods in development. We show that altering the epigenetic landscape by deleting CHD4 early during otic development (E8.5-E10.5) affects pathfinding and connectivity of SGN peripheral axons at multiple steps during axon guidance and may contribute to hearing loss in SIHIWES.

Although the phenotype is robust, penetrance is variable. We believe this is a central aspect observed in mutations of chromodomain helicase DNA-binding proteins. Cellular heterogeneity may contribute to the variable phenotype. There are four distinct subtypes of SGNs: type Ia, Ib, Ic and type II (Petitpre et al., 2018; Shrestha et al., 2018; Sun et al., 2022). CHD4 may function differently in each neuronal subtype, resulting in differing cellular phenotypes. The difference is evident in the axon guidance phenotypes observed in type I compared to type II neurons. Ablation of CHD4 affected the fasciculation of radial fibers and branching in the inner spiral plexus region for type I SGNs. In contrast, type II neurons displayed a circuitous path to innervate the base of outer hair cells and inappropriate turning at the outer hair cell region. Deleting CHD4 affected the peripheral axons differently in type I and II SGNs.

In addition to the heterogeneity of neuronal subtypes, variability within type I and II fibers was also observed. The phenotypic variability includes the extent of type I radial fiber bundling and branching of terminals in the inner spiral plexus. CHD4 function in SGN type Ia, b, and c fibers may contribute to the observed variability. Cellular heterogeneity, however, cannot be attributed to the improper turning of some type II peripheral axons. Some type II fibers are seemingly unaffected, whereas others turn in the opposite direction. Stochasticity in molecular processes may be a contributing mechanism. Stochastic gene expression involves biochemical processes such as transcription and translation. The limiting

number of molecules that catalyze transcription leads to biological variability, as observed by the dramatic differences in transcript levels even within isogenic cells (Raj and van Oudenaarden, 2008). Deletion of CHD4 may alter the chromatin state of cis-regulatory elements and impact the stochasticity in transcription. The epigenetic perturbation could increase both transcript levels and the variance of specific genes after ablating CHD4. We showed an increase in the median number of *Epha4* transcripts in *Calb2* marked SGNs concomitant with an increase in the variance of the transcript numbers. The increase in transcripts and variance was specific for *Epha4* and not *Calb2*. The larger variance results in a broader distribution of neurons with *Epha4* and displays a cell population that exceeds the normal range of *Epha4* levels in control SGNs. The percentage of neurons with increased *Epha4* transcripts may possess altered EPHA4 protein expression and perturb axon guidance. In contrast, cells that retain *Epha4* transcripts within the normal range retain normal axon pathfinding. The increase in transcriptional variance may contribute to the heterogeneous cellular phenotypes observed for type I and type II SGNs.

We identified multiple axon guidance deficits of type I and II SGNs using a *Chd4* conditional knockout mouse model. These deficits likely arise at different developmental time points and implicate CHD4 function at varying steps of SGN pathfinding. The candidate CHD4 binding sites include promoters and enhancers that regulate the transcription of Eph receptors and Ephrin ligands. CHD4 and the NuRD subunits HDAC1/2 may impose a repressive epigenetic state on these cis-regulatory elements to attenuate transcription. Inactivation of CHD4 increases transcript levels of axon guidance genes to perturb the stereotypic peripheral axon patterning. These results also have a broader implication on other neuronal circuits in patients with SIHIWES, where subtle changes may be more challenging to define.

Conflict of Interest:

The authors declared no potential conflicts of interest to the research, authorship, and publication of this article.

Accession Numbers:

The GEO accession number for the CUT&Tag raw fastq data, along with the processed bigwig and SEACR peak files, is GSE250033. IGV session with the CUT&Tag tracks can be provided upon request.

Author contribution:

JK and EM designed, performed experiments, acquired and analyzed immunofluorescent images. JN performed CUT&Tag and JQ analyzed data from CUT&Tag. KYK assisted in data analysis on CUT&Tag and RNAscope. KYK conceived the project and assisted with the analysis. JK, EM, and KYK wrote the manuscript.

Acknowledgments:

We thank Dr. Katia Georgopoulos (Mass General Hospital) and Dr. Lisa Goodrich (Harvard Medical School) for providing the *Chd4*$^{flox/flox}$ animals and advice on dosing the Ngn1 CreER^{T2} animals, respectively. We acknowledge Dr. Alejandra Laureano and Ms. Anna Maria Hinman for initially generating and maintaining the mouse line. NIH R01 DC015000 supported this work to KYK.

Fig. 1

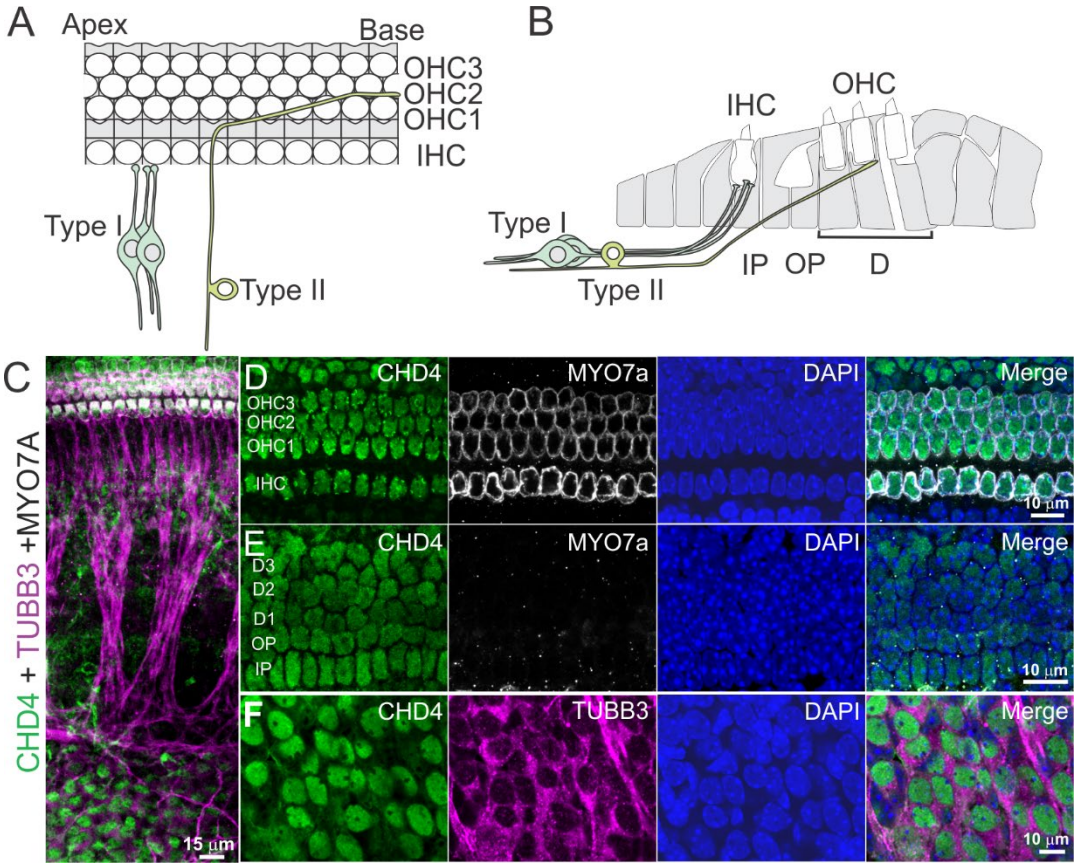

Fig. 2

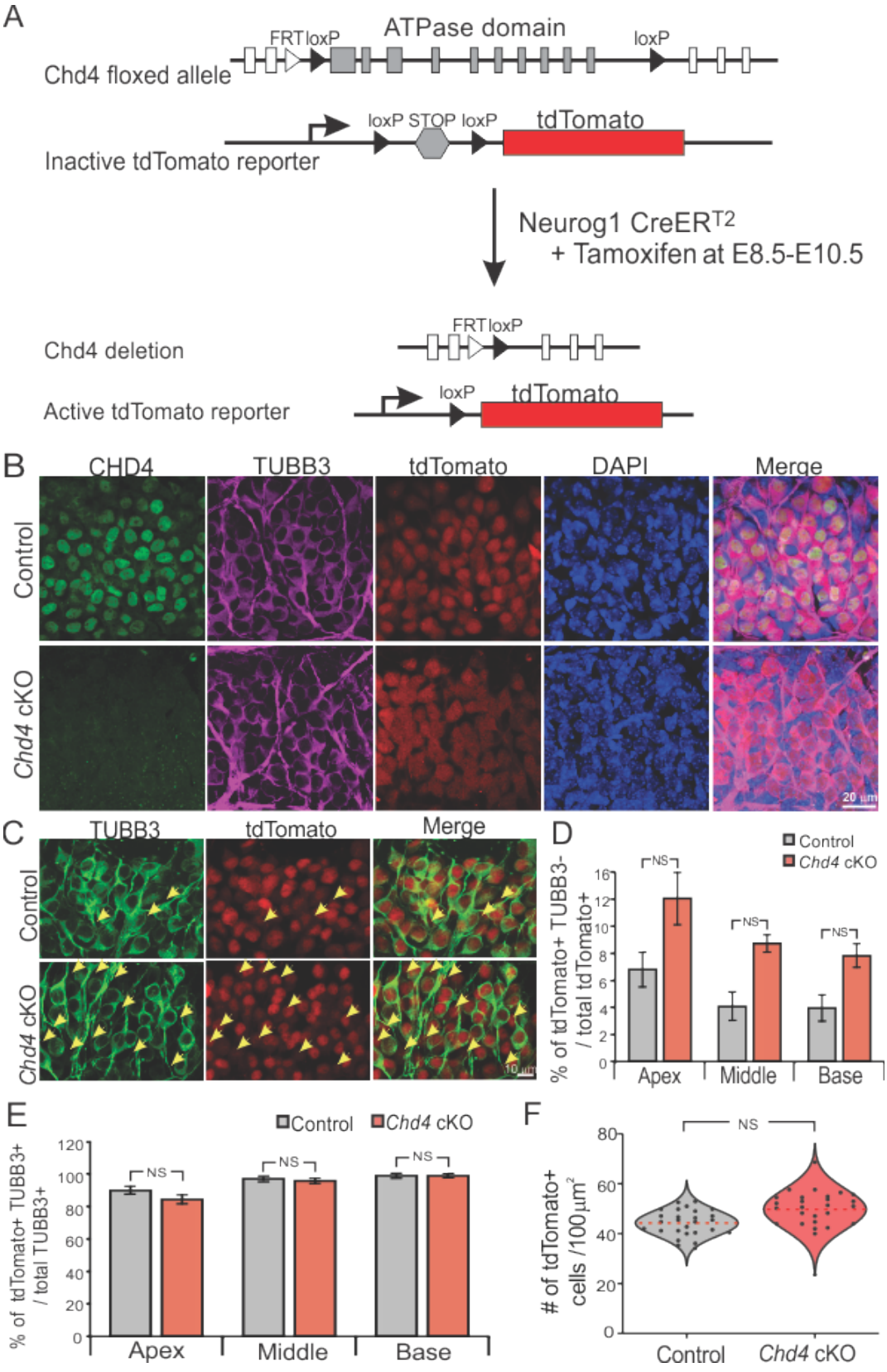

Figure 3

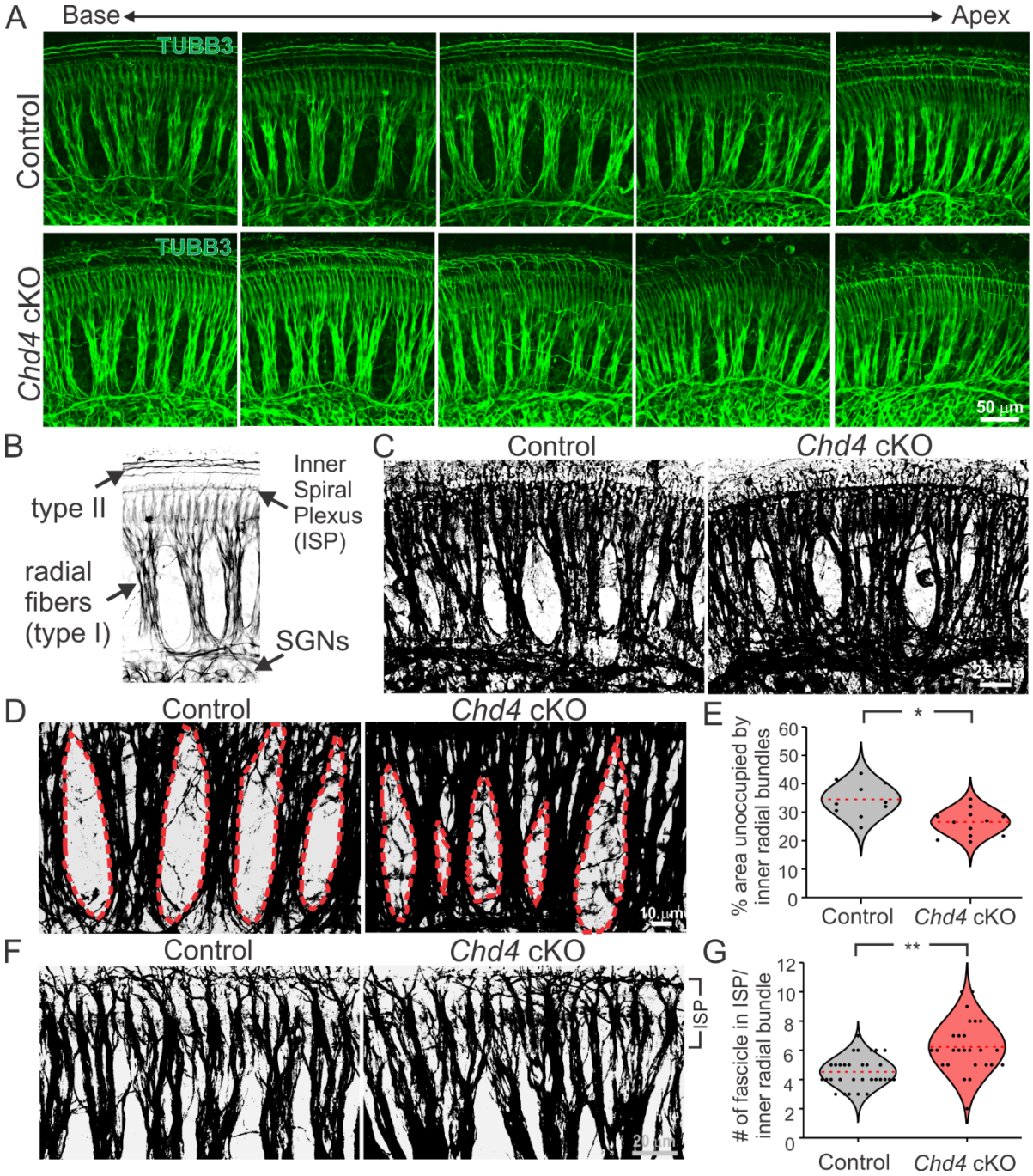

Figure 4.

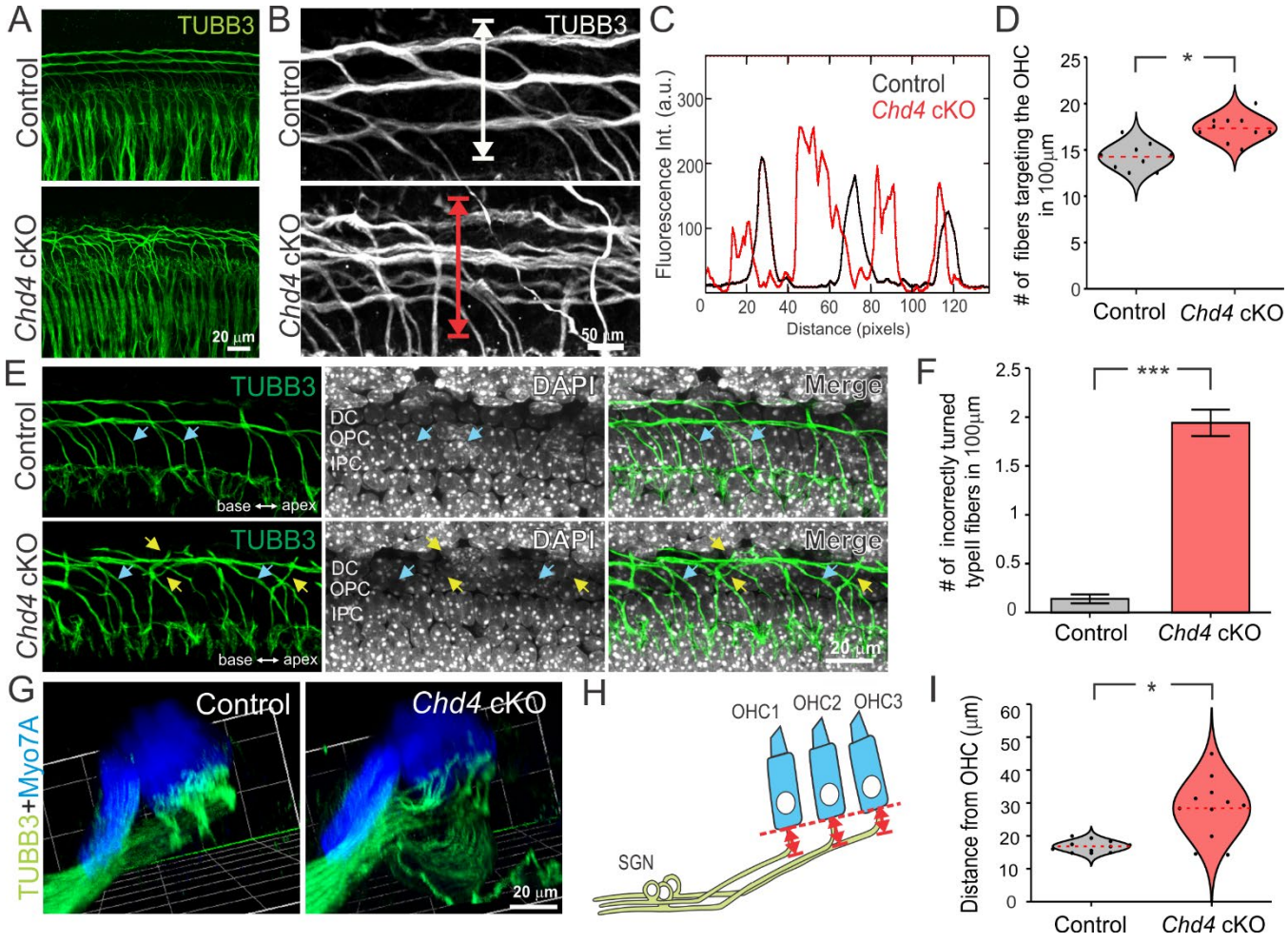

Figure 5

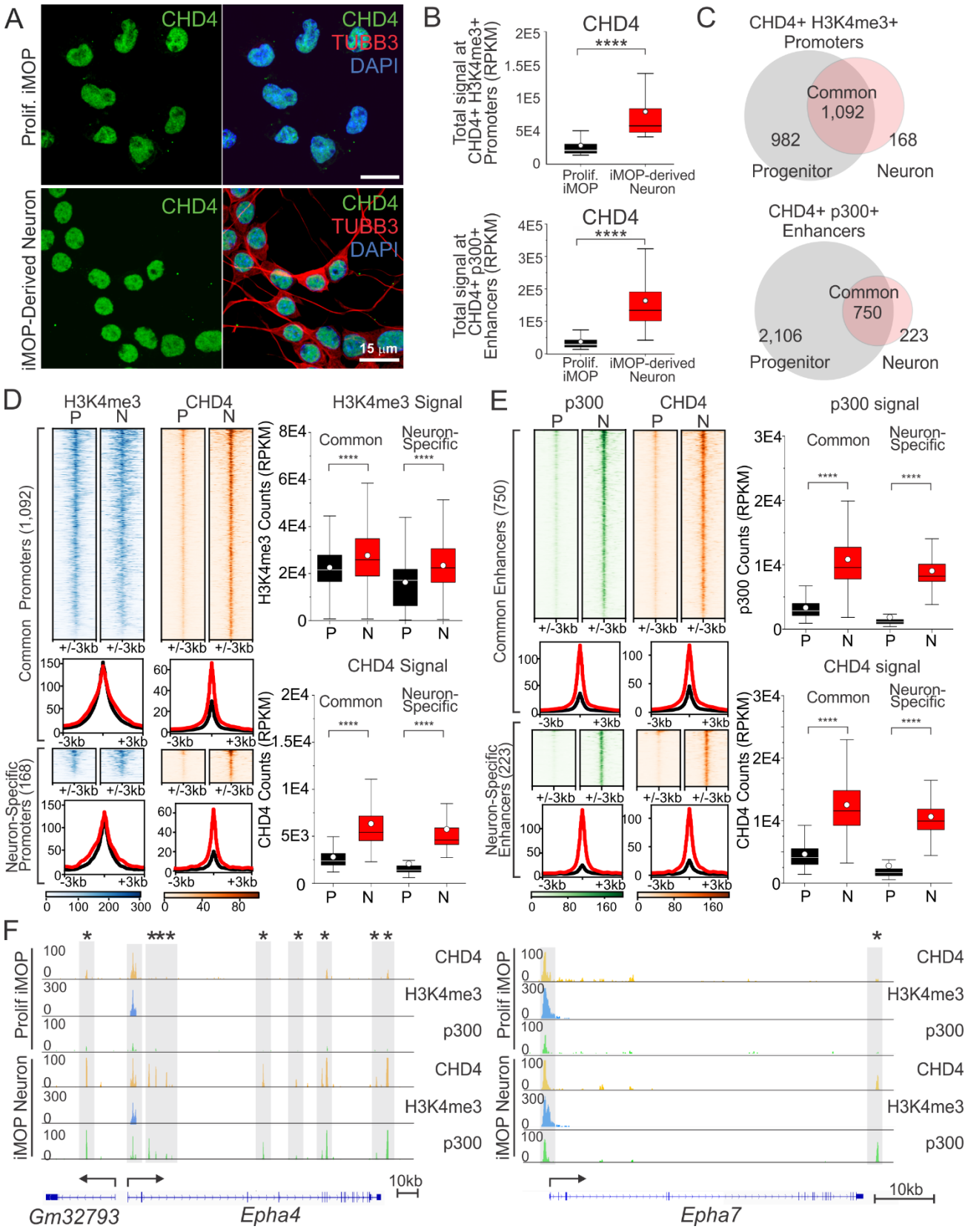

Figure 6.

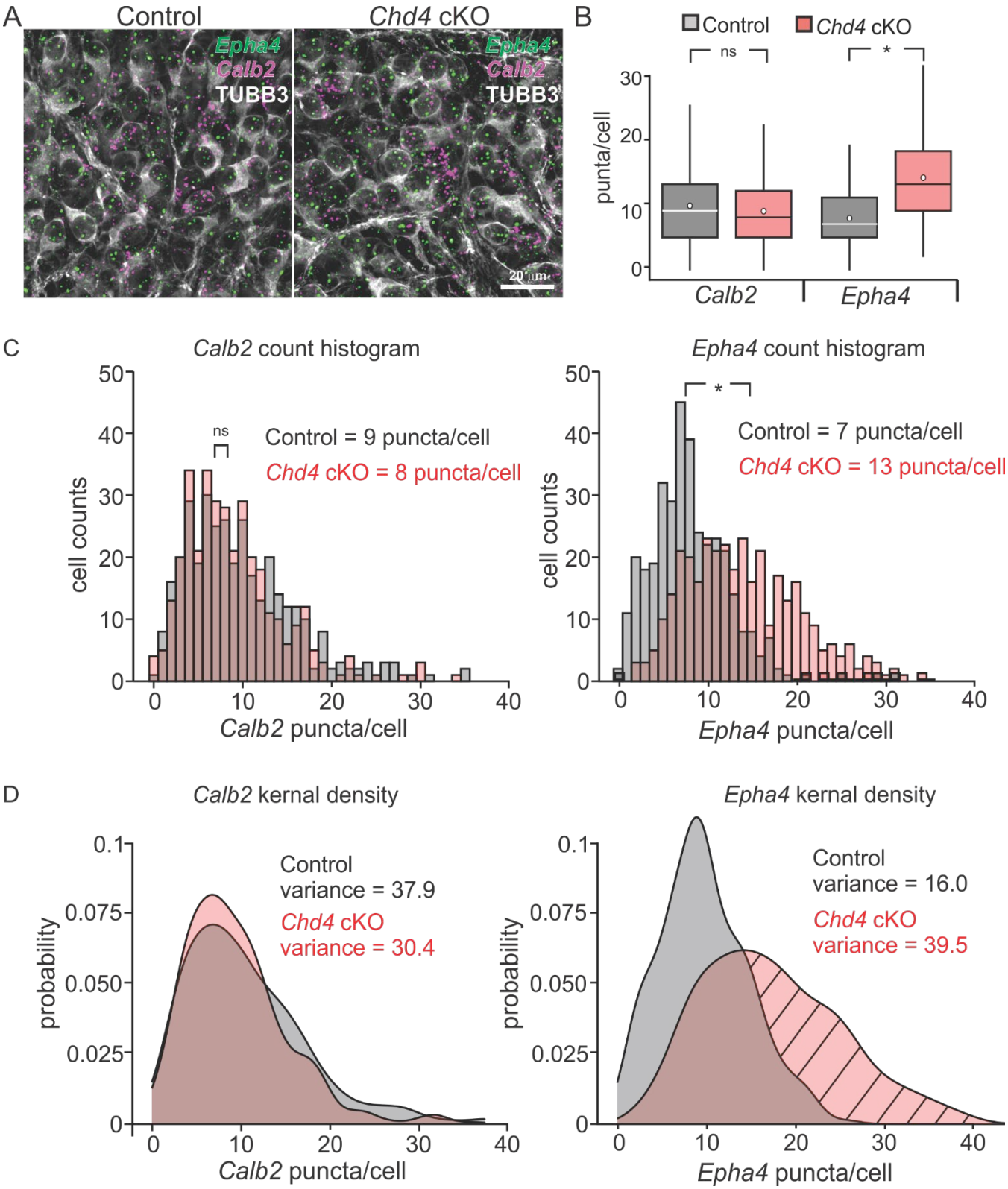

Figure 1. CHD4 expression in the spiral ganglion and the organ of Corti.

(A) Top-down schematic depicting the innervation pattern of type I and II SGNs. Type I SGNs extend single, unbranched neurites that innervate an individual inner hair cell (IHC). Type II SGNs extend neurites into the outer hair cell (OHC) region, turn basally, and can contact multiple OHCs. (B) Sagittal schematic of the innervation pattern. Multiple Type I SGNs innervate a single IHC. Type II neurites make a basal turn in the region near Deiters' cells, a supporting cell type. (C) Immunofluorescence labeling of CHD4 (green), TUBB3 (magenta), and MYO7A (white) from a flat-mounted cochlea. TUBB3 and MYO7A label neurons and hair cells, while DAPI (blue) marks nuclei. Different regions of immunolabeled E18.5 cochlea. (D) Expression of CHD4 in the single row of inner hair cells (IHC) and the three rows of outer hair cells (OHC1-3). (E) CHD4 labeling in supporting cells, including inner pillar (IP), outer pillar (OP), and three rows of Dieter cells (DC1-3). The nuclei of supporting cells reside underneath hair cells. (F) CHD4 labeling in spiral ganglion neurons. Scale bar as marked.

Figure 2. Deletion of *Chd4* from SGNs using Neurog1 CreER^{T2} Chd4 $^{flox/flox}$ mice.

(A) Schematic illustration of Cre-mediated *Chd4* deletion following tamoxifen induction in *Chd4* conditional knockout (cKO) mice containing Neurog1 CreER^{T2}; *Chd4*$^{flox/flox}$; tdTomato alleles. Administration of tamoxifen at E8.5-E10.5 deletes loxP flanked exons coding for the *Chd4* ATPase domain and activates expression of the tdTomato reporter. Animals without the *Chd4* cKO allele (Neurog1 CreER^{T2}; tdTomato) were used as controls (B) Immunostaining of CHD4 and TUBB3 marked neurons in E18.5 cochlea. tdTomato expression correlates with the presence of Cre activity. Nuclear CHD4 expression was observed in DAPI-marked nuclei in control SGNs but was absent in *Chd4* cKO SGNs after tamoxifen administration. (C) Confocal micrographs from the spiral ganglion. Yellow arrows indicate tdTomato^{+} and TUBB3^{-} cells. (D) Percentages of tdTomato^{+} and TUBB3^{-} cells found within the apex, middle, and base regions of the cochlea (apex, $p<0.136$, middle, $p<0.095$; base, $p<0.148$; control, n=3 and Chd4 cKO, n=3 cochlea) (E) Percentages of cells expressing tdTomato and TUBB3 from the base to apex of the cochlea from control and *Chd4* cKO cochleae (apex $p<0.302$; middle $p<0.603$; base,

p<0.9; control, n=3 and Chd4 cKO, n=3 cochleae) (F) Normalized number of tdTomato$^+$ cells per 100 μm^2 area in control and Chd4 cKO cochleae (p<0.081; control, n=27 and *Chd4* cKO n=27 images were analyzed from control, n=3 and *Chd4* cKO, n=3 cochleae).The Student's t-test test was used for statistical analysis using the number of cochleae. Scale bar as marked.

Figure 3. Inner radial bundles display fasciculation defects in *Chd4* cKO cochleae

(A) TUBB3 labeled cochleae from E18.5 control and *Chd4* cKO animals. Images are ordered from base to apex. (B) Depiction of the inner spiral plexus (ISP) near the base of inner hair cells and peripheral projections from type I (radial fibers) and II SGNs from E18.5 cochlea. (C) Binarized images of TUBB3 labeled control and *Chd4* cKO cochleae at E18.5. (D) Regions between radial fiber bundles were outlined in red. (E) The identified areas were quantified and compared between control and *Chd4* cKO (p<0.049; control, n=10 and *Chd4* cKO n=13 images were analyzed from control, n=3 and *Chd4* cKO, n=3 cochleae). (F) Binarized images of control and *Chd4* cKO E18.5 cochleae around the ISP. (G) Comparison of the normalized number of fascicles in the ISP per radial bundle between control and *Chd4* cKO cochleae (p<0.008; control, n=31 and *Chd4* cKO n=26 bundles were analyzed from control, n=5 and *Chd4* cKO, n=3 cochleae). The Student's t-test was used for statistical analysis. Scale bars as marked.

Figure 4. Type II spiral ganglion neurons display turning defects in the *Chd4* cKO mice.

(A) TUBB3 labeled neuronal projections in E18.5 control and *Chd4* cKO cochleae**.** Type II fibers can be distinguished by their anatomical location. (B) Type II fibers from control show stereotypic tracks that turn towards the base and travel along individual rows of outer hair cells. *Chd4* cKO type II fibers showed aberrant fiber tracks. (C) The intensity profile plot was measured along the white and red lines to highlight the differences between the control and Chd4 cKO fiber tracks. Peaks from fluorescence intensity measurements indicate the presence of a fiber track. Control cochleae show three peaks correlating with fibers along the three rows of outer hair cells. Chd4 cKO samples showed an additional peak suggesting aberrant fiber tracks (D) Normalized number of fibers entering the OHC region per 100 µm from control

and *Chd4* cKO E18.5 cochleae ($p<0.027$; control, n=9 and *Chd4* cKO n=10 images were analyzed from control, n=3 and *Chd4* cKO, n=3 cochleae). (E) Optical section from TUBB3 and DAPI labeled confocal micrographs that visualize fibers entering the OHC region. Blue arrows mark correctly turned while yellow arrows show incorrect turning type II fibers. (F) The normalized number of incorrectly turned type II fibers per 100 µm from control and *Chd4* cKO E18.5 cochleae ($p=2.82 \times 10^{-4}$; control, n=3 and *Chd4* cKO, n=3 cochleae). (G) 3D-rendered images highlighting the axonal trajectory from SGNs ($TUBB3^+$, green) to hair cells ($MYO7A^+$, blue). (H) Schematic of peripheral SGN axonal projections to outer hair cells. Red arrows represent the distance between contact points in the OHCs (red dashed line) and the final turning point on the incoming axon. (I) Average distances from the base of outer hair cells to the axon bundles showed differences between control and *Chd4* cKO ($p<0.034$; control, n=11, and *Chd4* cKO n=11 images were analyzed from control, n=3 and *Chd4* cKO, n=3 cochleae). The Student's t-test was used for statistical analysis. Scale bars as marked.

Figure 5. CHD4 binds to the promoters of genes involved in axon guidance, including members of the ephrin family of signaling molecules, in iMOP-derived neurons.

(A) Overlap of CHD4 in the nuclei (DAPI) of proliferating iMOP and TUBB3 labeled iMOP-derived neurons. CUT&Tag was performed using proliferating iMOP cells and iMOP-derived neurons. CUT&Tag peaks were identified using SEACR. (B) Box and whisker plots show SEACR total signals for CHD4 at CHD4+ H3K4me3+ and CHD4+p300+ in proliferating iMOPs were significantly different from that in iMOP-derived neurons, $p<2.2 \times 10^{-16}$. (C) Venn diagrams show the overlap of CHD4+ H3K4me3+ promoters and CHD4+ p300+ enhancers between progenitors (P) and neurons (N). (D) Heatmaps and profile plots show H3K4me3 and CHD4 signals within +/- 3kb of the summit regions of common and neuron-specific promoters. Box and whisker plots show significantly increased H3K4me3 and CHD4 signals at both common and neuron-specific promoters in P compared to N. (E) Heatmaps and profile plots show p300 and CHD4 signals within +/- 3kb of the summit regions of common and neuron-specific enhancers. Box and whisker plots showing significantly increased p300 and CHD4 signals at both

762 common and neuron-specific enhancers in P compared to that in N. (F) Enrichment of CHD4 (orange),
763 H3K4me3 (blue), and p300 (green) at the specified genomic region of *Epha4* and *Epha7* in proliferating
764 iMOPs and iMOP-derived neurons. Highlighted genomic regions represent H3K4me3 marked promoters.
765 Highlighted regions with asterisks denote the regions with increased enrichment of CHD4 and p300 in
766 iMOP-derived neurons. The number of asterisks denotes the peaks with increased CHD4 and p300
767 levels. Wilcoxon rank-sum test was used for statistical analysis. Scale bars as marked.
768
769 **Figure 6. *Chd4* cKO shows increased *Epha4* mRNA expression in SGNs.**
770 (A) E16.5 control and mutant cochlea processed for RNA fluorescence *in situ* hybridization (FISH) with
771 probes against *Epha4* and *Calb2.* Cochleae were immunolabeled with TUBB3 to visualize SGNs. (B) The
772 number of puncta for individual TUBB3 labeled cells was quantified. The lines denoted median values,
773 and the circles represented mean values. Controls were compared to *Chd4* cKO samples after
774 performing smFISH for *Calb2* ($p<0.295$) and Epha4 ($p<0.011$; control, n=3 and *Chd4* cKO, n=3 cochlea).
775 *Calb2* was used as a transcript to mark the SGNs, while *Epha4* was used as a CHD4 target gene.
776 Distribution of the number of smFISH puncta in control and *Chd4* cKO SGNs for (C) *Calb2* and *Epha4*
777 transcripts in SGNs (control, n=350 and *Chd4* cKO n=345 cells were counted from control, n=3 and *Chd4*
778 cKO, n=3 cochleae). (D) Kernal densities for *Calb2* and *Epha4* transcripts. Significant non-overlapping
779 regions of densities in Epha4 (hashed region) display an increased probability of cells from Chd4 cKO
780 with higher levels of Epha4 transcripts compared to the control. Wilcoxon rank-sum test was used for
781 statistical analysis. Scale bars as marked.
782

Fig. S1

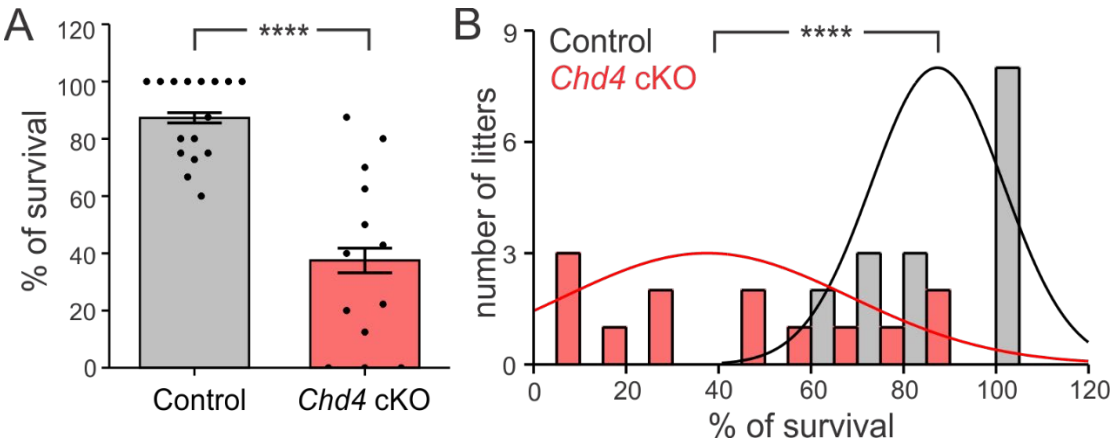

Fig. S2

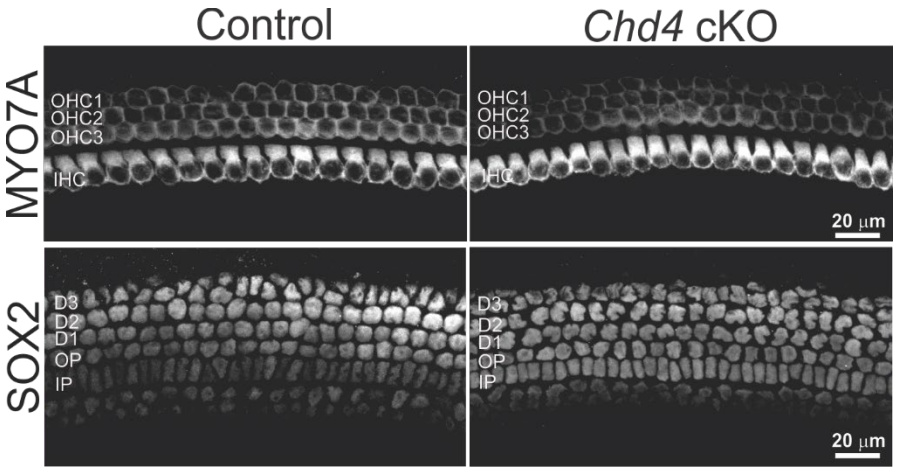

Fig. S3

A

ID	Description	p value
0048013	ephrin receptor signaling pathway	4.9E-05
0007411	axon guidance	2.0E-13
1902287	semaphorin-plexin signaling pathway involved in axon guidance	2.7E-02
0007409	axonogenesis	1.6E-14
0006325	chromatin organization	5.1E-14
0007413	axonal fasciculation	1.6E-02

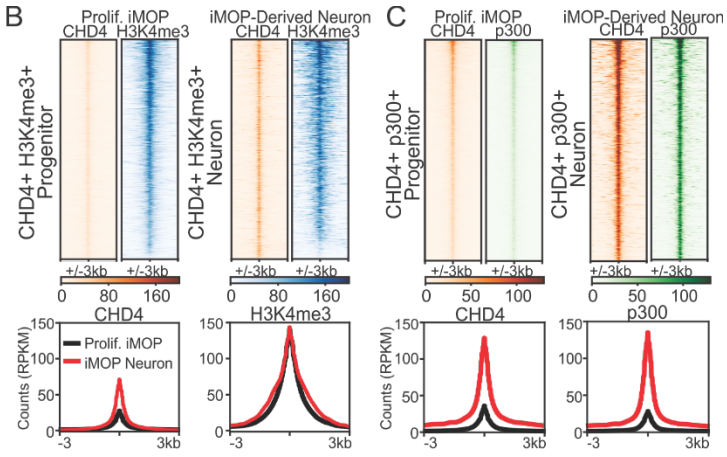

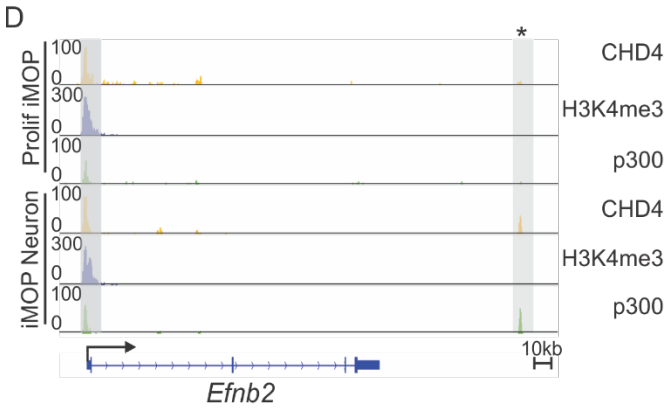

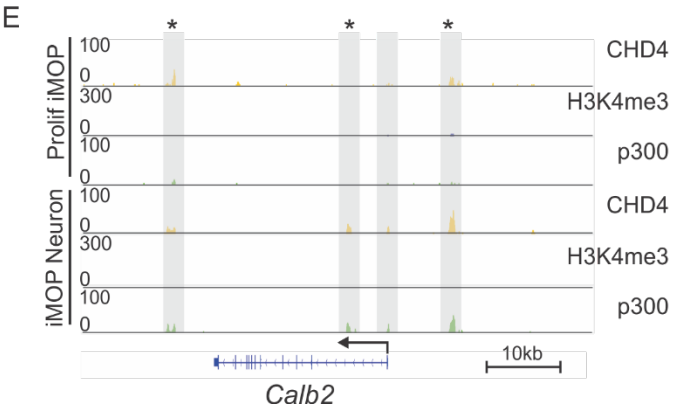

Supplemental Figure Legend

Supplemental Figure 1. Survival of *Chd4* conditional knockout mice.

(A) Average percentage of viable pups from all collected control and mutant litters ($p<4.36 \times 10^{-6}$; control, n=16 and *Chd4* cKO, n=13 litters). (B) Distribution of the percentages of surviving E18.5 pups from control and *Chd4* cKO litters after tamoxifen treatment. The p-value and sample size as listed. The Student's t-test was used for statistical analysis.

Supplemental Figure 2. The number of supporting and hair cells is unaffected following the deletion of *Chd4* within spiral ganglion neurons.

Immunofluorescent labeling of MYO7A and SOX2 marked hair cells and supporting cells from E18.5 cochleae. Confocal stacks from control and *Chd4* cKO cochleae with MYO7A marked hair cells and SOX2 marked supporting cells. OHC = outer hair cell, IHC = inner hair cell, D = Deiters' cells, OP = outer phalangeal cells, IP = inner phalangeal cells. Scale bar as marked.

Supplemental Figure 3. Identifying CHD4 binding at promoters and enhancers of target genes.

(A) Table showing Gene Ontology ID, description of each category, and corresponding adjusted p values using Benjamini-Hochberg method for multiple testing correction. (B) Heatmaps and profile plots of CHD4 and H3K4me3 signals within +/- 3kb of the summit regions of CHD4+ H3K4me3+ in both proliferating iMOP and iMOP-derived neurons. (C) Heatmaps and profile plots of CHD4 and p300 signals within +/- 3kb of the summit regions of CHD4+ p300+ in prolif. iMOP and iMOP-derived neurons. (D Enrichment of CHD4 (orange), H3K4me3 (blue), and p300 (green) at the specified genomic regions of *Efnb2* in proliferating iMOPs and iMOP-derived neurons. Highlighted genomic regions represented H3K4me3 marked promoters, while highlighted regions with asterisks denote regions with increased CHD4 and p300 in iMOP-derived neurons. The number of asterisks indicate the number of peaks that show increased CHD4 and p300 levels. Scale bars as marked.

Table 1

Allele	Sequence (5'->3')	Amplicon Size
Chd4	TCC AGA AGA AGA CGG CAG AT	Wild-type: 275bp Chd4 floxed allele: 400bp
	CTG GTC ATA GGG CAG GTC TC	
Ai9 tdTomato	AAG GGA GCT GCA GTG GAG TA	Wild-type: 287bp
	CCG AAA ATC TGT GGG AAG TC	
	GGC ATT AAA GCA GCG TAT CC	Mutant: 196bp
	CTG TTC CTG TAC GGC ATG G	
Generic Cre	AGC GAT CGC TGC CAG GAT	Mutant: 382bp
	ACC AGC GTT TTC GTT CTG CC	
Neurogenin1-specific Cre	AGC CCA TTC ACT CCC TGA G	Mutant: 527bp
	ATC AAC GTT TTC TTT TCG GA	

Table 2

Antibody	Company	Identifier	Dilution	Purpose
mouse anti-CHD4	Abcam	Cat# ab70469, RRID:AB_2229454	1:100 (tissue) 1:300 (cells)	Immunostaining
rabbit anti-MYO7A	Proteus Bioscience	Cat# 25-6790, RRID:AB_10015251	1:200	Immunostaining
mouse anti-Tuj1 (TUBB3)	BioLegend	Cat# 801202, RRID:AB_10063408	1:300	Immunostaining
rabbit anti-Tuj1 (TUBB3)	BioLegend	Cat# 802001, RRID:AB_2564645	1:300	Immunostaining
rabbit anti-Sox2	Millipore	Cat# AB5603, RRID:AB_2286686	1:100	Immunostaining
goat anti-mouse Alexa 488	Thermo Fisher Scientific	Cat# A-11001, RRID:AB_2534069	1:500	Immunostaining
goat anti-mouse Alexa 647	Thermo Fisher Scientific	Cat# A-21235, RRID:AB_2535804	1:500	Immunostaining
goat anti-rabbit Alexa 488	Thermo Fisher Scientific	Cat# A-11034, RRID:AB_2576217	1:500	Immunostaining
goat anti-rabbit Alexa 647	Thermo Fisher Scientific	Cat# A-21246, RRID:AB_2535814	1:500	Immunostaining
goat anti-rabbit Alexa 568	Thermo Fisher Scientific	Cat# A-11011, RRID:AB_143157	1:500	Immunostaining
Rabbit anti-EP300 (p300)	Developmental Studies Hybridoma Bank (DSHB)	Cat# ENCITp300-1, RRID:AB_2619604	1:50	CUT&Tag
rabbit anti-H3K4me3	Active Motif	Cat# 39060, RRID: AB_2615077	1:50	CUT&Tag
Rabbit anti-CHD4	Abcam	Cat# ab72418, RRID:AB_1268107	1:50	CUT&Tag
rabbit IgG	Jackson ImmunoResearch	Cat# 011-000-003, RRID:AB_2337118	1:50	CUT&Tag

Table 3

RNAscope Probe	Accession Number	Probe Region	Catalog Number
Mm-Calb2	NM_007586.1	147-1265	313641
Mm-Epha4	NM_007936.3	291-1191	419081

References

Adamson, C. L., Reid, M. A., Mo, Z. L., Bowne-English, J. and Davis, R. L. (2002). Firing features and potassium channel content of murine spiral ganglion neurons vary with cochlear location. *J Comp Neurol* **447**, 331-350.

Appler, J. M. and Goodrich, L. V. (2011). Connecting the ear to the brain: Molecular mechanisms of auditory circuit assembly. *Prog Neurobiol* **93**, 488-508.

Borg, E., Engstrom, B., Linde, G. and Marklund, K. (1988). Eighth nerve fiber firing features in normal-hearing rabbits. *Hear Res* **36**, 191-201.

Bornelov, S., Reynolds, N., Xenophontos, M., Gharbi, S., Johnstone, E., Floyd, R., Ralser, M., Signolet, J., Loos, R., Dietmann, S., et al. (2018). The Nucleosome Remodeling and Deacetylation Complex Modulates Chromatin Structure at Sites of Active Transcription to Fine-Tune Gene Expression. *Mol Cell* **71**, 56-72 e54.

Bruce, L. L., Kingsley, J., Nichols, D. H. and Fritzsch, B. (1997). The development of vestibulocochlear efferents and cochlear afferents in mice. *Int J Dev Neurosci* **15**, 671-692.

Chen, W. C., Xue, H. Z., Hsu, Y. L., Liu, Q., Patel, S. and Davis, R. L. (2011). Complex distribution patterns of voltage-gated calcium channel alpha-subunits in the spiral ganglion. *Hear Res* **278**, 52-68.

Clapier, C. R., Iwasa, J., Cairns, B. R. and Peterson, C. L. (2017). Mechanisms of action and regulation of ATP-dependent chromatin-remodelling complexes. *Nat Rev Mol Cell Biol* **18**, 407-422.

Coate, T. M., Raft, S., Zhao, X., Ryan, A. K., Crenshaw, E. B., 3rd and Kelley, M. W. (2012). Otic mesenchyme cells regulate spiral ganglion axon fasciculation through a Pou3f4/EphA4 signaling pathway. *Neuron* **73**, 49-63.

Coate, T. M., Spita, N. A., Zhang, K. D., Isgrig, K. T. and Kelley, M. W. (2015). Neuropilin-2/Semaphorin-3F-mediated repulsion promotes inner hair cell innervation by spiral ganglion neurons. *Elife* **4**.

Deans, M. R. (2022). Planar cell polarity signaling guides cochlear innervation. *Dev Biol* **486**, 1-4.

Defourny, J., Poirrier, A. L., Lallemend, F., Mateo Sanchez, S., Neef, J., Vanderhaeghen, P., Soriano, E., Peuckert, C., Kullander, K., Fritzsch, B., et al. (2013). Ephrin-A5/EphA4 signalling controls specific afferent targeting to cochlear hair cells. *Nat Commun* **4**, 1438.

el Barbary, A. (1991). Auditory nerve of the normal and jaundiced rat. I. Spontaneous discharge rate and cochlear nerve histology. *Hear Res* **54**, 75-90.

Ghimire, S. R. and Deans, M. R. (2019). Frizzled3 and Frizzled6 Cooperate with Vangl2 to Direct Cochlear Innervation by Type II Spiral Ganglion Neurons. *J Neurosci* **39**, 8013-8023.

Ghimire, S. R., Ratzan, E. M. and Deans, M. R. (2018). A non-autonomous function of the core PCP protein VANGL2 directs peripheral axon turning in the developing cochlea. *Development* **145**.

Hoffmeister, H., Fuchs, A., Erdel, F., Pinz, S., Grobner-Ferreira, R., Bruckmann, A., Deutzmann, R., Schwartz, U., Maldonado, R., Huber, C., et al. (2017). CHD3 and CHD4 form distinct NuRD complexes with different yet overlapping functionality. *Nucleic Acids Res* **45**, 10534-10554.

Hosokawa, H., Tanaka, T., Suzuki, Y., Iwamura, C., Ohkubo, S., Endoh, K., Kato, M., Endo, Y., Onodera, A., Tumes, D. J., et al. (2013). Functionally distinct Gata3/Chd4 complexes coordinately establish T helper 2 (Th2) cell identity. *Proc Natl Acad Sci U S A* **110**, 4691-4696.

Huang, D., Sherman, B. T. and Lempicki, R. A. (2009). Systematic and integrative analysis of large gene lists using DAVID bioinformatics resources. *Nat Protoc* **4**, 44-57.

Huang, L. C., Barclay, M., Lee, K., Peter, S., Housley, G. D., Thorne, P. R. and Montgomery, J. M. (2012). Synaptic profiles during neurite extension, refinement and retraction in the developing cochlea. *Neural Dev* **7**, 38.

Hung, H., Kohnken, R. and Svaren, J. (2012). The nucleosome remodeling and deacetylase chromatin remodeling (NuRD) complex is required for peripheral nerve myelination. *J Neurosci* **32**, 1517-1527.

Kent, W. J., Zweig, A. S., Barber, G., Hinrichs, A. S. and Karolchik, D. (2010). BigWig and BigBed: enabling browsing of large distributed datasets. *Bioinformatics* **26**, 2204-2207.

Kiang, N. Y., Pfeiffer, R. R., Warr, W. B. and Backus, A. S. (1965). Stimulus Coding in the Cochlear Nucleus. *Ann Otol Rhinol Laryngol* **74**, 463-485.

Kim, E. J., Hori, K., Wyckoff, A., Dickel, L. K., Koundakjian, E. J., Goodrich, L. V. and Johnson, J. E. (2011). Spatiotemporal fate map of neurogenin1 (Neurog1) lineages in the mouse central nervous system. *J Comp Neurol* **519**, 1355-1370.

Kim, Y. J., Ibrahim, L. A., Wang, S. Z., Yuan, W., Evgrafov, O. V., Knowles, J. A., Wang, K., Tao, H. W. and Zhang, L. I. (2016). EphA7 regulates spiral ganglion innervation of cochlear hair cells. *Dev Neurobiol* **76**, 452-469.

Koundakjian, E. J., Appler, J. L. and Goodrich, L. V. (2007). Auditory neurons make stereotyped wiring decisions before maturation of their targets. *J Neurosci* **27**, 14078-14088.

Kwan, K. Y., Shen, J. and Corey, D. P. (2015). C-MYC transcriptionally amplifies SOX2 target genes to regulate self-renewal in multipotent otic progenitor cells. *Stem Cell Reports* **4**, 47-60.

Langmead, B. and Salzberg, S. L. (2012). Fast gapped-read alignment with Bowtie 2. *Nat Methods* **9**, 357-359.

Layman, W. S., Sauceda, M. A. and Zuo, J. (2013). Epigenetic alterations by NuRD and PRC2 in the neonatal mouse cochlea. *Hear Res* **304**, 167-178.

Layman, W. S. and Zuo, J. (2014). Epigenetic regulation in the inner ear and its potential roles in development, protection, and regeneration. *Front Cell Neurosci* **8**, 446.

Li, H., Handsaker, B., Wysoker, A., Fennell, T., Ruan, J., Homer, N., Marth, G., Abecasis, G., Durbin, R. and Genome Project Data Processing, S. (2009). The Sequence Alignment/Map format and SAMtools. *Bioinformatics* **25**, 2078-2079.

Liberman, M. C. (1978). Auditory-nerve response from cats raised in a low-noise chamber. *J Acoust Soc Am* **63**, 442-455.

---- (1982). Single-neuron labeling in the cat auditory nerve. *Science* **216**, 1239-1241.

Liu, Q., Manis, P. B. and Davis, R. L. (2014). I h and HCN channels in murine spiral ganglion neurons: tonotopic variation, local heterogeneity, and kinetic model. *J Assoc Res Otolaryngol* **15**, 585-599.

Liu, W. and Davis, R. L. (2014). Calretinin and calbindin distribution patterns specify subpopulations of type I and type II spiral ganglion neurons in postnatal murine cochlea. *J Comp Neurol* **522**, 2299-2318.

Low, J. K., Webb, S. R., Silva, A. P., Saathoff, H., Ryan, D. P., Torrado, M., Brofelth, M., Parker, B. L., Shepherd, N. E. and Mackay, J. P. (2016). CHD4 Is a Peripheral Component of the Nucleosome Remodeling and Deacetylase Complex. *J Biol Chem* **291**, 15853-15866.

Lu, C. C., Appler, J. M., Houseman, E. A. and Goodrich, L. V. (2011). Developmental profiling of spiral ganglion neurons reveals insights into auditory circuit assembly. *J Neurosci* **31**, 10903-10918.

Madisen, L., Zwingman, T. A., Sunkin, S. M., Oh, S. W., Zariwala, H. A., Gu, H., Ng, L. L., Palmiter, R. D., Hawrylycz, M. J., Jones, A. R., et al. (2010). A robust and high-throughput Cre reporting and characterization system for the whole mouse brain. *Nat Neurosci* **13**, 133-140.

Martinez-Monedero, R., Liu, C., Weisz, C., Vyas, P., Fuchs, P. A. and Glowatzki, E. (2016). GluA2-Containing AMPA Receptors Distinguish Ribbon-Associated from Ribbonless Afferent Contacts on Rat Cochlear Hair Cells. *eNeuro* **3**.

Meers, M. P., Bryson, T. D., Henikoff, J. G. and Henikoff, S. (2019a). Improved CUT&RUN chromatin profiling tools. *Elife* **8**.

Meers, M. P., Tenenbaum, D. and Henikoff, S. (2019b). Peak calling by Sparse Enrichment Analysis for CUT&RUN chromatin profiling. *Epigenetics Chromatin* **12**, 42.

Micucci, J. A., Sperry, E. D. and Martin, D. M. (2015). Chromodomain helicase DNA-binding proteins in stem cells and human developmental diseases. *Stem Cells Dev* **24**, 917-926.

Millard, C. J., Varma, N., Saleh, A., Morris, K., Watson, P. J., Bottrill, A. R., Fairall, L., Smith, C. J. and Schwabe, J. W. (2016). The structure of the core NuRD repression complex provides insights into its interaction with chromatin. *Elife* **5**, e13941.

Morra, R., Lee, B. M., Shaw, H., Tuma, R. and Mancini, E. J. (2012). Concerted action of the PHD, chromo and motor domains regulates the human chromatin remodelling ATPase CHD4. *FEBS Lett* **586**, 2513-2521.

Nitarska, J., Smith, J. G., Sherlock, W. T., Hillege, M. M., Nott, A., Barshop, W. D., Vashisht, A. A., Wohlschlegel, J. A., Mitter, R. and Riccio, A. (2016). A Functional Switch of NuRD Chromatin Remodeling Complex Subunits Regulates Mouse Cortical Development. *Cell Rep* **17**, 1683-1698.

Pan, M. R., Hsieh, H. J., Dai, H., Hung, W. C., Li, K., Peng, G. and Lin, S. Y. (2012). Chromodomain helicase DNA-binding protein 4 (CHD4) regulates homologous recombination DNA repair, and its deficiency sensitizes cells to poly(ADP-ribose) polymerase (PARP) inhibitor treatment. *J Biol Chem* **287**, 6764-6772.

Petitpre, C., Wu, H., Sharma, A., Tokarska, A., Fontanet, P., Wang, Y., Helmbacher, F., Yackle, K., Silberberg, G., Hadjab, S., et al. (2018). Neuronal heterogeneity and stereotyped connectivity in the auditory afferent system. *Nat Commun* **9**, 3691.

Polo, S. E., Kaidi, A., Baskcomb, L., Galanty, Y. and Jackson, S. P. (2010). Regulation of DNA-damage responses and cell-cycle progression by the chromatin remodelling factor CHD4. *EMBO J* **29**, 3130-3139.

Quinlan, A. R. and Hall, I. M. (2010). BEDTools: a flexible suite of utilities for comparing genomic features. *Bioinformatics* **26**, 841-842.

Raft, S., Koundakjian, E. J., Quinones, H., Jayasena, C. S., Goodrich, L. V., Johnson, J. E., Segil, N. and Groves, A. K. (2007). Cross-regulation of Ngn1 and Math1 coordinates the production of neurons and sensory hair cells during inner ear development. *Development* **134**, 4405-4415.

Raj, A. and van Oudenaarden, A. (2008). Nature, nurture, or chance: stochastic gene expression and its consequences. *Cell* **135**, 216-226.

Ramirez, F., Dundar, F., Diehl, S., Gruning, B. A. and Manke, T. (2014). deepTools: a flexible platform for exploring deep-sequencing data. *Nucleic Acids Res* **42**, W187-191.

Robinson, J. T., Thorvaldsdottir, H., Winckler, W., Guttman, M., Lander, E. S., Getz, G. and Mesirov, J. P. (2011). Integrative genomics viewer. *Nat Biotechnol* **29**, 24-26.

Ruggero, M. A., Santi, P. A. and Rich, N. C. (1982). Type II cochlear ganglion cells in the chinchilla. *Hear Res* **8**, 339-356.

Sanders, T. R. and Kelley, M. W. (2022). Specification of neuronal subtypes in the spiral ganglion begins prior to birth in the mouse. *Proc Natl Acad Sci U S A* **119**, e2203935119.

Schmiedt, R. A. (1989). Spontaneous rates, thresholds and tuning of auditory-nerve fibers in the gerbil: comparisons to cat data. *Hear Res* **42**, 23-35.

Shrestha, B. R., Chia, C., Wu, L., Kujawa, S. G., Liberman, M. C. and Goodrich, L. V. (2018). Sensory Neuron Diversity in the Inner Ear Is Shaped by Activity. *Cell* **174**, 1229-1246 e1217.

Sifrim, A., Hitz, M. P., Wilsdon, A., Breckpot, J., Turki, S. H., Thienpont, B., McRae, J., Fitzgerald, T. W., Singh, T., Swaminathan, G. J., et al. (2016a). Distinct genetic architectures for syndromic and nonsyndromic congenital heart defects identified by exome sequencing. *Nat Genet* **48**, 1060-1065.

Sifrim, A., Hitz, M. P., Wilsdon, A., Breckpot, J., Turki, S. H., Thienpont, B., McRae, J., Fitzgerald, T. W., Singh, T., Swaminathan, G. J., et al. (2016b). Distinct genetic architectures for syndromic and nonsyndromic congenital heart defects identified by exome sequencing. *Nat Genet* **48**, 1060-1065.

Spoendlin, H. (1972). Innervation densities of the cochlea. *Acta Otolaryngol* **73**, 235-248.

Sun, Y., Wang, L., Zhu, T., Wu, B., Wang, G., Luo, Z., Li, C., Wei, W. and Liu, Z. (2022). Single-cell transcriptomic landscapes of the otic neuronal lineage at multiple early embryonic ages. *Cell Rep* **38**, 110542.

Taberner, A. M. and Liberman, M. C. (2005). Response properties of single auditory nerve fibers in the mouse. *J Neurophysiol* **93**, 557-569.

Tong, J. K., Hassig, C. A., Schnitzler, G. R., Kingston, R. E. and Schreiber, S. L. (1998). Chromatin deacetylation by an ATP-dependent nucleosome remodelling complex. *Nature* **395**, 917-921.

Torchy, M. P., Hamiche, A. and Klaholz, B. P. (2015). Structure and function insights into the NuRD chromatin remodeling complex. *Cell Mol Life Sci* **72**, 2491-2507.

Toriello, H. V., Reardon, W., Gorlin, R. J. and Gorlin, R. J. (2004). *Hereditary hearing loss and its syndromes* (2nd edn). Oxford ; New York: Oxford University Press.

Torrado, M., Low, J. K. K., Silva, A. P. G., Schmidberger, J. W., Sana, M., Sharifi Tabar, M., Isilak, M. E., Winning, C. S., Kwong, C., Bedward, M. J., et al. (2017). Refinement of the subunit interaction network within the nucleosome remodelling and deacetylase (NuRD) complex. *FEBS J* **284**, 4216-4232.

Watson, A. A., Mahajan, P., Mertens, H. D., Deery, M. J., Zhang, W., Pham, P., Du, X., Bartke, T., Zhang, W., Edlich, C., et al. (2012). The PHD and chromo domains regulate the ATPase activity of the human chromatin remodeler CHD4. *J Mol Biol* **422**, 3-17.

Weiss, K., Lazar, H. P., Kurolap, A., Martinez, A. F., Paperna, T., Cohen, L., Smeland, M. F., Whalen, S., Heide, S., Keren, B., et al. (2020). The CHD4-related syndrome: a comprehensive investigation of the clinical spectrum, genotype-phenotype correlations, and molecular basis. *Genet Med* **22**, 389-397.

Weiss, K., Terhal, P. A., Cohen, L., Bruccoleri, M., Irving, M., Martinez, A. F., Rosenfeld, J. A., Machol, K., Yang, Y., Liu, P., et al. (2016). De Novo Mutations in CHD4, an ATP-Dependent Chromatin Remodeler Gene, Cause an Intellectual Disability Syndrome with Distinctive Dysmorphisms. *Am J Hum Genet* **99**, 934-941.

Williams, C. J., Naito, T., Arco, P. G., Seavitt, J. R., Cashman, S. M., De Souza, B., Qi, X., Keables, P., Von Andrian, U. H. and Georgopoulos, K. (2004). The chromatin remodeler Mi-2beta is required for CD4 expression and T cell development. *Immunity* **20**, 719-733.

Winter, I. M., Robertson, D. and Yates, G. K. (1990). Diversity of characteristic frequency rate-intensity functions in guinea pig auditory nerve fibres. *Hear Res* **45**, 191-202.

Xia, L., Huang, W., Bellani, M., Seidman, M. M., Wu, K., Fan, D., Nie, Y., Cai, Y., Zhang, Y. W., Yu, L. R., et al. (2017). CHD4 Has Oncogenic Functions in Initiating and Maintaining Epigenetic Suppression of Multiple Tumor Suppressor Genes. *Cancer Cell* **31**, 653-668 e657.

Xue, Y., Wong, J., Moreno, G. T., Young, M. K., Cote, J. and Wang, W. (1998). NURD, a novel complex with both ATP-dependent chromatin-remodeling and histone deacetylase activities. *Mol Cell* **2**, 851-861.

Yang, Y., Yamada, T., Hill, K. K., Hemberg, M., Reddy, N. C., Cho, H. Y., Guthrie, A. N., Oldenborg, A., Heiney, S. A., Ohmae, S., et al. (2016). Chromatin remodeling inactivates activity genes and regulates neural coding. *Science* **353**, 300-305.

Yoshida, T., Hu, Y., Zhang, Z., Emmanuel, A. O., Galani, K., Muhire, B., Snippert, H. J., Williams, C. J., Tolstorukov, M. Y., Gounari, F., et al. (2019). Chromatin restriction by the nucleosome remodeler Mi-2beta and functional interplay with lineage-specific transcription regulators control B-cell differentiation. *Genes Dev* **33**, 763-781.

Zhang, K. D. and Coate, T. M. (2017). Recent advances in the development and function of type II spiral ganglion neurons in the mammalian inner ear. *Semin Cell Dev Biol* **65**, 80-87.

Zhang, Y., LeRoy, G., Seelig, H. P., Lane, W. S. and Reinberg, D. (1998). The dermatomyositis-specific autoantigen Mi2 is a component of a complex containing histone deacetylase and nucleosome remodeling activities. *Cell* **95**, 279-289.

Zhu, L. J., Gazin, C., Lawson, N. D., Pages, H., Lin, S. M., Lapointe, D. S. and Green, M. R. (2010). ChIPpeakAnno: a Bioconductor package to annotate ChIP-seq and ChIP-chip data. *BMC Bioinformatics* **11**, 237.